

RESEARCH

Open Access



# Carboxymethyl-sagocellulose-stabilized Fe<sub>3</sub>O<sub>4</sub> nanoparticles with 5-fluorouracil as photothermal agents for tumor ablation

Anand Kumar Veeramachineni<sup>1</sup>, Thenapakiam Sathasivam<sup>2,3</sup>, Ragul Paramasivam<sup>1</sup>, Saravanan Muniyandy<sup>4</sup>, Shafii Bin Khamis<sup>5</sup>, Yau Yan Lim<sup>1</sup> and Janarthanan Pushpamalar<sup>1,3\*</sup>

\*Correspondence:  
pushpa.janarthanan@monash.edu;  
pjanarth72@gmail.com

<sup>1</sup> School of Science, Monash University Malaysia, Jalan Lagoon Selatan, Bandar Sunway, 47500 Subang Jaya, Selangor Darul Ehsan, Malaysia

<sup>2</sup> School of Pharmacy, Monash University Malaysia, Jalan Lagoon Selatan, Bandar Sunway, 47500 Subang Jaya, Selangor Darul Ehsan, Malaysia

<sup>3</sup> Monash-Industry Plant Oils Research Laboratory (MIPO), Monash University Malaysia, Jalan Lagoon Selatan, Bandar Sunway, 47500 Subang Jaya, Selangor Darul Ehsan, Malaysia

<sup>4</sup> Department of Pharmacy, Fatima College of Health Sciences, Al Maqam, Al Ain, United Arab Emirates

<sup>5</sup> Medical Technology Division, Malaysian Nuclear Agency, 43000 Bangi, Selangor Darul Ehsan, Malaysia

## Abstract

**Background:** There is a continuous growth of interest in the development of nano-drug delivery systems that could combine therapy and diagnosis of cancer.

**Results:** Novel multifunctional superparamagnetic iron oxide nanoparticles (SPIONs, chemically Fe<sub>3</sub>O<sub>4</sub>) conjugated with carboxymethyl sagocellulose (CMSC), and 5-fluorouracil (Fe<sub>3</sub>O<sub>4</sub>-CMSC-5FU) were synthesized. The conjugated nanoparticles have the magnetic properties of the SPIONs, which allows the nanoparticles to be localized at the target area by applying an external magnetic field. SPIONs generate heat upon exposure to laser lights, resulting in a photothermic effect. The drug-loading efficiency of 5-FU into the SPIONs-CMSC conjugated nanoparticles was 70 to 84% w/w which could release the drug at intracellular pH (5.4) of cancer cells and resist drug release at pH 7.2. In vivo studies using mice models confirmed the nanoparticles could efficiently deliver 5-FU only to the cancer cells and the anticancer effect was enhanced by laser-induced hyperthermia.

**Conclusions:** The combination of targeted delivery of 5-FU with photothermal therapy (PTT) looks promising for selective killing of cancer cells. Furthermore, SPIONs are an excellent contrasting agent for use in computerized tomography (CT) imaging for determining the tumor location and monitoring the progress of the therapy. The focus of this work was the oncological application of multifunctional Fe<sub>3</sub>O<sub>4</sub>-CMSC-5FU nanoparticle conjugates, with an emphasis on therapeutic, diagnostic and prognostic purposes.

**Keywords:** Carboxymethyl sagocellulose, Drug delivery system, pH-responsive, Photothermal therapy, Magnetic nanoparticles, In vivo thermal ablation

## Background

Currently, there is a continuous growth of interest in the development of nano-drug delivery systems that could combine therapy and diagnosis of cancer (Xu et al. 2015). Compared with existing cancer therapies such as radiotherapy and chemotherapy, near infra-red (NIR) light-induced photothermal therapy (PTT) with imaging-guided cancer therapy has gained more attention because there are no adverse effects on the patient



©The Author(s) 2024. **Open Access** This article is licensed under a Creative Commons Attribution 4.0 International License, which permits use, sharing, adaptation, distribution and reproduction in any medium or format, as long as you give appropriate credit to the original author(s) and the source, provide a link to the Creative Commons licence, and indicate if changes were made. The images or other third party material in this article are included in the article's Creative Commons licence, unless indicated otherwise in a credit line to the material. If material is not included in the article's Creative Commons licence and your intended use is not permitted by statutory regulation or exceeds the permitted use, you will need to obtain permission directly from the copyright holder. To view a copy of this licence, visit <http://creativecommons.org/licenses/by/4.0/>. The Creative Commons Public Domain Dedication waiver (<http://creativecommons.org/publicdomain/zero/1.0/>) applies to the data made available in this article, unless otherwise stated in a credit line to the data.

after the treatment (Chen et al. 2021). One recent trend involves the development of multifunctional nanoparticles capable of both delivering therapeutic agents to cancer cells and providing imaging for diagnosis purposes (Madamsetty et al. 2019). The combinatorial treatment approach using nanoparticles and NIR light irradiation convert the photon energy to thermal energy, causing the ablation of the cancer cell (Yu et al. 2015). The targeted treatment to cancer cells is effective with minimal damage to the healthy cells (Motofei 2023). Intensive studies on various PTT agents have been reported (Fernandes et al. 2021a, b). However,  $\text{Fe}_3\text{O}_4$  nanoparticles have gained an advantage owing to their response to an external magnetic field and NIR irradiation (Adam and Mertz 2023). The integration of hyperthermia therapies with drug delivery and MRI imaging represents a transformative approach in cancer treatment, offering unprecedented precision, efficacy, and real-time monitoring capabilities. Despite ongoing challenges, continued research efforts aimed at optimizing nanoparticle properties and addressing technical barriers hold the promise of unlocking the full therapeutic potential of these multifunctional nanostructures. External magnetic field helpful in anchoring  $\text{Fe}_3\text{O}_4$  nanoparticles at target site and irradiation helps to generate heat at the target site.

Many drug delivery systems have been developed using SPIONs, which also exhibit improved magnetic resonance imaging (MRI) (Stanicki et al. 2022). Iron oxide nanoclusters (Chauhan and Kushwaha 2021), liposomes (Kato et al. 2015), micelles (Sun et al. 2016), polysomes (Bertrand et al. 2015) are some of the delivery systems that have exhibited higher MRI contrast compared to commercially available products (Hola et al. 2015). The SPIONs have garnered significant interest for their biocompatibility, minimal toxicity and their responsiveness to magnetic fields, making them ideal candidates for drug delivery vehicles (Hooshmand et al. 2021). Moreover, the commercially available products fail to localize in tumor tissue, causing toxic effects to normal cells.

Unlike healthy tissue, cancerous tissue possesses leaky vasculature with enhanced permeability and retention (EPR) effect (Danhier et al. 2018) that can be exploited for easy uptake of nanoparticles. It has also been demonstrated that the rapid magnetic response and great mass magnetization of the modified iron oxide nanoclusters is extremely favorable for achieving a high surface area for drug loading (Hola et al. 2015). Moreover,  $\text{Fe}_3\text{O}_4$  has been proven to be an effective negative contrast agent for  $T_2$ -weighted ( $T_2$ WI) MRI (Lu et al. 2022; Yang et al. 2023). This facilitates high spatial resolution and noninvasive tracking of cancer cells, providing high precision on producing signals for deep cancer tissue imaging. A well-dispersed and homogeneous solution of magnetic nanoparticles with an increased stability can be obtained by suitable surface modification (Kango et al. 2013; Stark et al. 2015). The surface modification is vital as it varies the physiochemical properties of the nanoparticles including the size, magnetization power and dispersion (Hooshmand et al. 2021), which influences the cell uptake, bio-distribution and mimics the innate immunity (Monopoli et al. 2020). Recently, surface modifications using organic and inorganic metal oxides and bio-macromolecules have been extensively investigated (Kango et al. 2013). Surface modifications for clinical applications are mostly performed with carbohydrate polymers that simulate glycoproteins in a biological system (Hamidi et al. 2013). The choice of cancer treatment such as chemotherapy, radiation therapy, and surgery, varies widely based on the site of origin/location. A clinically approved, minimally invasive therapeutic method called photodynamic

therapy (PDT) has the ability to specifically target and kill cancerous cells (Agostinis et al. 2011). A photosensitizing agent is administered, and then the patient is exposed to radiation at a wavelength that matches an absorbance band of the photosensitizer. Direct tumor cell death, microvasculature harm, and the initiation of a local inflammatory response all occur in the presence of oxygen. PDT can be curative, according to clinical studies, especially for early-stage tumors. It can significantly raise quality of life and extend survival in cancer patients who are not candidates for surgery. This treatment is an excellent therapeutic option for combination therapies due to its low normal tissue toxicity, negligible systemic effects, significantly decreased long-term morbidity, lack of inherent or acquired resistance mechanisms, and excellent cosmetic and organ function-preserving effects. On top of the recent advances in PDT (Xu et al. 2015), using metallic nanoparticles made up of gold and silver can be used to treat all forms of cancer (Yang et al. 2016), irrespective of its location.

Fluorouracil (5-FU) is widely used for the treatment of cancer, including breast, aerodigestive tract and colorectal cancer (Choong and Vokes 2008). The combination of 5-FU with PDT has proved to have the greatest therapeutic impact for colon cancer. In addition, an improved chemotherapeutic response was observed when 5-FU combined with other drugs for breast, head and neck cancer (Gramont et al. 1997).

Several researchers have used various carbohydrate polymers such as chitosan, dextrin and carboxymethyl cellulose (CMC) for the synthesis of polymer-drug nanocarriers for cancer treatment. The use of CMCs for surface coating of metal nanoparticles (NPs) has proved more effective for stabilization of the nanoparticles (Yu et al. 2015; Dominguez-Brauer et al. 2015; Espinosa et al. 2016).

In this study, magnetic nanoparticles were successfully synthesized by a simple solvothermal method.  $\text{Fe}_3\text{O}_4$  NPs were surface-modified with poly(4-styrenesulfonic acid-co-maleic acid) (PSSMA) to facilitate amino-functionalization with (3-aminopropyl) triethoxysilane (APS). Subsequently, the amino-functionalized  $\text{Fe}_3\text{O}_4$  NPs were conjugated with carboxymethyl chitosan (CMSC) for stabilization and biocompatibility and 5-FU for cancer therapy. The ability to use these nanoparticles for magnetic targeting and as agents for PTT and MRI/CT contrasting was demonstrated both *in vitro* and *in vivo*. Photothermal ablation of cancer cells by magnetic targeting was achieved by using 808-nm NIR laser irradiation and an external magnetic field. The  $\text{Fe}_3\text{O}_4$ -CMSC-5FU exhibited excellent targeting efficiency as a 5-FU carrier as well as effective PTT for combinational cancer treatment.

## Materials and methods

### Chemicals and reagents

Sodium hydroxide pellets (97%), sodium monoacetate (98%), sodium chlorite (80% technical grade), acetic acid (99.9%), acetone (99.6%), isopropanol (99.9%), ethanol (absolute), chloroform, sulphuric acid (98.7%), formic acid, hydrogen peroxide (30%), ferric chloride hexahydrate ( $\text{FeCl}_3 \cdot 6\text{H}_2\text{O}$ ) and poly(4-styrenesulfonic acid-co-maleic acid, SS/MA = 3:1) sodium salt (PSSMA, MW = 20,000 g/mol), sodium acetate trihydrate ( $\text{CH}_3\text{COONa} \cdot 3\text{H}_2\text{O}$ ), 1-ethyl-3-(3-dimethylaminopropyl) carbodiimide (EDC) and *N*-hydroxysulfosuccinimide (sulfo-NHS) were purchased from Sigma-Aldrich, USA. The aminopropyltriethoxysilane (APS) and 5-fluorouracil (5-FU) were obtained from Nacalai

Tesque (Japan). All other reagents and chemicals were analytical grade and used without further purification. Deionized (DI) water was used throughout the experiments.

### Measurements and characterizations

An 808-nm infrared laser module with an adjustable focus of 2 W/cm<sup>2</sup> power density (ECLIPSERA Co., Ltd., Czech Republic) was used for the experiments. The morphology and structure of the prepared Fe<sub>3</sub>O<sub>4</sub> particles were characterized on an *SU8010* field emission scanning electron microscope (FESEM) with energy-dispersive X-ray spectroscopy (EDX) and a transmission electron microscope (TEM) (Philips CM-12) at an acceleration voltage of 80 kV. The dark-field STEM was performed using FESEM (SU8010) where the samples were prepared using a copper grid. However, the STEM is just a different mode of data acquiring method on FESEM. For FESEM is on the surface morphology analysis while for STEM the data acquired are from transmitted electron.

The FTIR spectra were measured between 600 and 4000 cm<sup>-1</sup> using a Varian 640-IR FTIR spectrophotometer. An X-ray diffractometer (D8-Advance Bruker-AXS) was used to investigate the phase behavior. The instrumental settings were set at 1.540 Å wavelength (CuK $\alpha$  radiation), with a scan speed of 2° per second and a 2 $\theta$  range of 2–90°.

The size distribution of the nanoparticles was measured on a Malvern Zetasizer Nano ZS90 instrument at room temperature, and a fold capillary cuvette (Folded Capillary Cell-DTS 1060, Malvern, UK) was equipped to measure the zeta charge of the samples. The nanoparticles were dispersed in distilled water by sonification. All the measurements were performed in triplicates.

### Syntheses of Fe<sub>3</sub>O<sub>4</sub> NPs

A modified solvothermal reaction was used to synthesize the magnetic Fe<sub>3</sub>O<sub>4</sub> nanoparticles. The PSSMA (1.0 g), FeCl<sub>3</sub>·6H<sub>2</sub>O (1.08 g) and NaOAc (3.0 g) were dissolved in 40 mL of ethylene glycol. After complete homogenization, the red-brown solution was subjected to the autoclave at 200 °C for 10 h. A black precipitate was formed, which was then washed with deionized water and dried at 30 °C overnight (Wei et al. 2015).

### Surface modification of Fe<sub>3</sub>O<sub>4</sub> NPs

The Fe<sub>3</sub>O<sub>4</sub> nanoclusters were amino-functionalized using (3-aminopropyl) triethoxysilane (APS). Briefly, the Fe<sub>3</sub>O<sub>4</sub> nanoparticles (0.60 g) were ultrasonically dispersed in 350 mL of ethanol and 3 mL of deionized water. Next, 4 mL of APS was added to the mixture solution and continuously stirred for 12 h under a N<sub>2</sub> atmosphere at room temperature (27 °C). A black precipitate was formed, which was then washed with deionized water, dried at 30 °C overnight and isolated as Fe<sub>3</sub>O<sub>4</sub>-NH<sub>2</sub> (Kato et al. 2015).

### Activation of CMSC using EDC and sulfo-NHS

The formation of an amide bond between the carboxylic groups of CMSC and the amine groups of the amino-functionalized Fe<sub>3</sub>O<sub>4</sub> nanoclusters was achieved in the presence of 1-ethyl-3-(3-dimethylaminopropyl) carbodiimide (EDC) and *N*-hydroxysulfosuccinimide (sulfo-NHS). A schematic diagram of the reaction is illustrated in Fig. 1A. An amine-reactive O-acylisourea intermediate compound was formed when EDC was reacted with

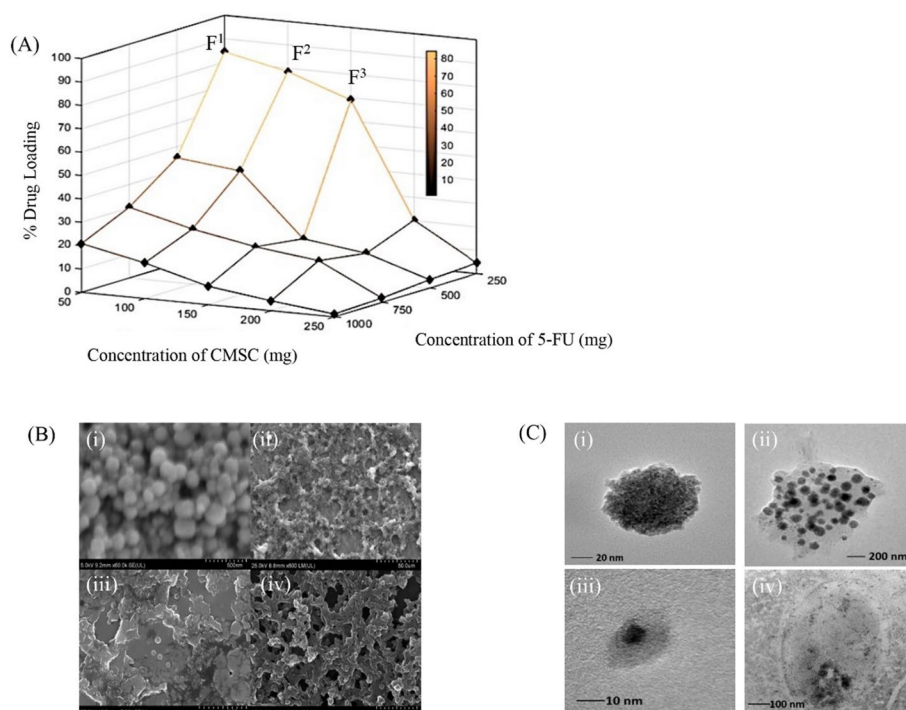


**Fig. 1** **A** The 3D graph of drug loading of 5-FU loaded Fe<sub>3</sub>O<sub>4</sub> nanocomplex. The FE-SEM images of **B** (i) Fe<sub>3</sub>O<sub>4</sub>-NH<sub>2</sub> nanoparticles, (ii) Fe<sub>3</sub>O<sub>4</sub>-5FU nanoparticles, (iii) Fe<sub>3</sub>O<sub>4</sub>-CMSC nanoparticles and (iv) Fe<sub>3</sub>O<sub>4</sub>-CMSC-5FU (Formulation F3) nanoparticles; **C** (i) and (ii) TEM images of Fe<sub>3</sub>O<sub>4</sub>-NH<sub>2</sub> nanoparticles, (iii) and (iv) TEM images of Fe<sub>3</sub>O<sub>4</sub>-CMSC-5FU (Formulation F3) nanoparticles

a carboxyl group, which was stabilized by sulfo-NHS, allowing the reaction with the primary amine of the Fe<sub>3</sub>O<sub>4</sub>-NH<sub>2</sub>.

The CMSC (1 g) was dissolved in 200 mL phosphate buffer solution (PBS) at pH 7.0 followed by the addition of EDC and sulfo-NHS at a molar ratio of 0.5 relative to the number of moles of the carboxyl groups of the polysaccharide. The reaction was then dialyzed 6 times against distilled water for 6 h to remove unreacted EDC and sulfo-NHS (Sun et al. 2016).

#### Synthesis of 5-FU functionalized with aldehyde

5-FU was modified using formalin (40% formaldehyde in an aqueous solution). Briefly, 1 g of 5-FU was dissolved in anhydrous dimethylsulfoxide (DMSO) by sonication. Formalin (10 mL) was then added, and the solution was stirred at 55 °C in the dark for 4 h (Fig. 1B). The sample was subjected to high vacuum for a week to remove all solvent present to ensure the purity of the sample. The sample was then dissolved in 10 mL of distilled dimethyl formamide and the solution was stored at − 15 °C until further use.

#### Synthesis of Fe<sub>3</sub>O<sub>4</sub>-NH<sub>2</sub> conjugated 5-FU stabilized with CMSC

A novel formulation was made by linking of the activated CMSC and functionalized 5-FU onto the Fe<sub>3</sub>O<sub>4</sub>-NH<sub>2</sub> by reacting the carboxylic groups of CMSC with the amino groups of Fe<sub>3</sub>O<sub>4</sub>-NH<sub>2</sub> through carbodiimide activation to form an amide II bond between the CMSC and amino groups of Fe<sub>3</sub>O<sub>4</sub>-NH<sub>2</sub> and an amine bond between

5-FU and  $\text{Fe}_3\text{O}_4\text{-NH}_2$ . An amine-reactive O-acylisourea intermediate was formed when EDC reacted with the carboxyl group of CMSC, which was stabilized by sulfon-NHS, allowing the reaction with the primary amine of the  $\text{Fe}_3\text{O}_4\text{-NH}_2$ . Briefly, 1.2 g of  $\text{Fe}_3\text{O}_4\text{-NH}_2$  nanoparticles were added to 10 mL of buffer A (0.003 M phosphate, pH 6.0, 0.1 M NaCl) and sonicated for 10 min. Then, 5 mL of EDC solution (0.025 g/mL in buffer A) was added, and the reaction mixture was sonicated for another 10 min. Finally, the CMSC solution dissolved in 10 mL of buffer A and the modified 5-FU solution was added to the above reaction mixture, sonicated and stirred for 12 h at room temperature in the dark. The  $\text{Fe}_3\text{O}_4\text{-CMSC-5FU}$  nanocomplex (Fig. 1C) was recovered from the reaction mixture by placing the bottle on a permanent magnet with a surface magnetization of 6000 G. The magnetic particles all settled within 1–2 min, were washed repeatedly with water and ethanol, and finally vacuum-dried at 30°C overnight.  $\text{Fe}_3\text{O}_4\text{-CMSC-5FU}$  was prepared with different amounts of CMSC and 5-FU to achieve high drug loading and drug release (Table 1).

The percentage of 5-FU loading in the  $\text{Fe}_3\text{O}_4\text{-CMSC-5FU}$  was determined by UV spectroscopy. Initial absorbance of the drug was determined in the reaction mixture. After completion of conjugation,  $\text{Fe}_3\text{O}_4\text{-CMSC-5FU}$  was collected using a magnet and the rinsed twice using deionized water (30 mL for each time) to remove the unbound 5-FU. The supernatant and washing liquid were collected for UV measurement to determine the loading amounts of 5-FU at 266 nm. The encapsulation efficiency and loading efficiency were determined using following equations:

**Table 1** Formulation for  $\text{Fe}_3\text{O}_4\text{-NH}_2$  conjugated 5-FU stabilized with CMSC

Formulation code	Mass of $\text{Fe}_3\text{O}_4\text{-NH}_2$ /mg	Mass of CMSC/mg	Mass of 5-FU/mg
F1	1200	50	248
F2	1200	100	248
F3	1200	150	248
F4	1200	200	248
F5	1200	250	248
F6	1200	50	500
F7	1200	100	500
F8	1200	150	500
F9	1200	200	500
F10	1200	250	500
F11	1200	50	750
F12	1200	100	750
F13	1200	150	750
F14	1200	200	750
F15	1200	250	750
F16	1200	50	1000
F17	1200	100	1000
F18	1200	150	1000
F19	1200	200	1000
F20	1200	250	1000

$$\% \text{ of Encapsulation} = \frac{(\text{Initial amount of drug added} - \text{amount of unbound drug}) \times 100}{\text{Initial amount of drug added}}$$

$$\% \text{ of Loading} = \frac{(\text{Initial amount of drug added} - \text{amount of unbound drug}) \times 100}{\text{Amount of Fe}_3\text{O}_4 - \text{CMSC} - 5\text{FU recovered}}$$

### Cellular evaluation of Fe<sub>3</sub>O<sub>4</sub>-CMSC-5-FU targeting ability

#### Cellular toxicity

The cell-targeting ability of Fe<sub>3</sub>O<sub>4</sub>-CMSC-5FU was evaluated using human epithelial carcinoma (HeLa) cells and human embryonic kidney 293 (HEK 293) cells, using a 3-(4,5-dimethylthiazol-2-yl)-2,5-diphenyltetrazolium bromide (MTT) assay. HeLa cells and HEK 293 cells were seeded in 96-well plates at a density of  $1 \times 10^4$  cells/well in 100  $\mu\text{L}$  cell culture medium and incubated overnight to obtain 75–80% confluence, respectively. The culture medium was then replaced with fresh, serum-free medium, and a series of samples of 5-FU, Fe<sub>3</sub>O<sub>4</sub>, Fe<sub>3</sub>O<sub>4</sub>-CMSC-5FU was added to the cells. Cells were incubated with 5-FU, Fe<sub>3</sub>O<sub>4</sub>, Fe<sub>3</sub>O<sub>4</sub>-CMSC-5FU at a concentration of 1 mg/mL with respect to the originally seeded cells at 37 °C. Cells were incubated for a further 72 h. A total of 10  $\mu\text{L}$  MTT solution (5 mg/mL) was added to the 100  $\mu\text{L}$  of culture medium in each well prior to incubation at 37 °C for 4 h. The MTT-containing medium was replaced with 100  $\mu\text{L}$  of solubilization solution dimethyl sulfoxide (DMSO). Finally, the absorbance was measured at 595 nm using a microplate reader (Infinite M200 PRO, Tecan Trading AG, Switzerland) with a reference filter of 650 nm. The viability of the non-treated control cells was arbitrarily defined as 100%. The experiment was repeated three times for each sample treatment. Cell viability (%) was calculated according to the following Eq. (1):

$$\% \text{ Cell viability} = \frac{[\text{OD}_{595}(\text{sample}) - \text{OD}_{650}(\text{sample})]}{[\text{OD}_{595}(\text{control}) - \text{OD}_{650}(\text{control})]} \times 100, \quad (1)$$

in which  $\text{OD}_{595}(\text{sample})$  and  $\text{OD}_{650}(\text{sample})$  represent measurements from the wells treated with 5-FU, Fe<sub>3</sub>O<sub>4</sub>, Fe<sub>3</sub>O<sub>4</sub>-CMSC-5FU nanocomplex and  $\text{OD}_{595}(\text{control})$  and  $\text{OD}_{650}(\text{control})$  represent measurements from the wells treated only with DMEM containing 10% fetal calf serum. A hemocytometer was used to count cells. Add 15–20  $\mu\text{L}$  of cell suspension between the hemocytometer and cover glass and the number of cells was counted in all four outer squares divide by four (the mean number of cells/square). The number of cells per square  $\times 10^4 =$  the number of cells/mL of suspension.

#### Cell uptake study

Fe<sub>3</sub>O<sub>4</sub> and Fe<sub>3</sub>O<sub>4</sub>-CMSC-5FU nanoparticles at various concentrations (1  $\mu\text{g}$  to 1 mg) were prepared by creating a dispersion in Dulbecco's modified Eagle's medium (DMEM). HeLa cell lines and HEK 293 cells were cultivated in DMEM, supplemented with 10% fetal calf serum, 100 units  $\text{mL}^{-1}$  penicillin, and 100  $\mu\text{g mL}^{-1}$  streptomycin, 4 mM L-glutamine under a 5% CO<sub>2</sub> and 95% humidified atmosphere at 37 °C. All cells were cultured in a fully humidified atmosphere containing 5% CO<sub>2</sub> at 37 °C. 800  $\mu\text{L}$  from a  $5 \times 10^5$  cells  $\text{mL}^{-1}$  cell suspension was seeded into each well of a 24-well tissue culture plate

and incubated for 48 h, and the cells were examined by light microscopy (EVOS, AMG, USA).

#### **Cellular photothermal therapy (PTT)**

HeLa cells and HEK 293 cells were used to analyze PTT *in vitro*. DMEM supplemented with 10% fetal bovine serum, 100 units mL<sup>-1</sup> penicillin and 100 µg mL<sup>-1</sup> streptomycin; 4 mM L-glutamine was utilized as the cell culture medium. Cells were cultured at 37 °C in a humidified atmosphere containing 5% CO<sub>2</sub> and 95% air. For the *in vitro* studies, cells were incubated with different concentrations of Fe<sub>3</sub>O<sub>4</sub>-CMSC-5FU and Fe<sub>3</sub>O<sub>4</sub> nanoparticles in a 96-well cell culture plate at 37 °C and 5% CO<sub>2</sub>. After internalization with Fe<sub>3</sub>O<sub>4</sub>-CMSC-5FU and Fe<sub>3</sub>O<sub>4</sub> nanoparticles for 12 h, the cells were washed 3 times with sterile PBS and irradiated using an 808 nm NIR laser at a power density of 2 W/cm<sup>2</sup> for 1–3 min. After irradiation, the cells were seeded into 96-well plates and incubated for 24 h. A cell viability assay using 3-(4,5-dimethylthiazol-2-yl)-2, 5-diphenyltetrazolium bromide (MTT) was used to determine the thermal ablation efficiency after PTT. The control group was used as a normalized controlled treatment for cell viability.

#### **Evaluation of the nanoparticles *in vivo* using xenograft murine model**

##### ***Xenograft murine model (BALB/c)***

Male BALB/c mice (20 g) were obtained from InVivos Pte. Ltd. and used under protocols approved by Universiti Kebangsaan Malaysia (UKM) Laboratory Animal Center (MONASH/2016/PUSHPAMALAR/28-JAN./721-MARCH-2016-MAY-2016) and Monash University field work approval (MARF/2106/084/FW) by Monash Animal Ethics Committee. The animals were acclimated to an individually ventilated caging system at a temperature ranging from 18 to 25 °C, with a relative humidity of 55% to 65% and a 12 h light/dark cycle, for 1 week before the experiments.

HeLa cells were cultured and resuspended in serum-free DMEM medium (20 µL). For anesthesia, ketamine + xylazine was prepared by adding 2 mL of xylazine (10 mg/mL stock) along with 5 mL of ketamine (200 mg/mL stock) to make 7 mL of stock solution with 92 mg/mL (ketamine + xylazine). One mL of stock solution was used and diluted with 9 mL of saline solution. The sample was administered at a concentration of 10 mL/kg, which is equivalent to 10 µL/g.

After anesthesia, 20 µL of the cell suspension containing  $1 \times 10^7$  cells were inoculated into the mice to form a subcutaneous xenograft tumor model. At 72 h post-inoculation, the mice were randomly divided into four groups: The labeled groups are (i) group treated with Fe<sub>3</sub>O<sub>4</sub>-CMSC-5FU ( $n=5$ ) and laser therapy, (ii) group treated with 100 mg/kg Fe<sub>3</sub>O<sub>4</sub>-CMSC-5FU and no laser therapy ( $n=5$ ), (iii) group treated with only laser therapy ( $n=5$ ), (iv) control group ( $n=5$ ) with no Fe<sub>3</sub>O<sub>4</sub>-CMSC-5FU and no laser therapy. Fe<sub>3</sub>O<sub>4</sub>-CMSC-5FU and DMSO/saline as a control were post-inoculated with an intravenous (I.V.) administered vehicle only after the tumor volumes reached 100 mm<sup>3</sup>. Selection of the dose was based on preliminary *in vitro* data.

##### ***Evaluation of biodistribution in mouse model***

Magnetic targeting studies were carried out in the murine model by understanding the biodistribution of indocyanine green (ICG)-labeled Fe<sub>3</sub>O<sub>4</sub>-CMSC nanoparticles. A

near-infrared dye, an ICG Labeling Kit—NH<sub>2</sub> (Dojindo Molecular Technologies, Inc., USA) was primarily used for the preparation of ICG-labeled Fe<sub>3</sub>O<sub>4</sub>-CMSC nanoparticles. A 13-mm-diameter neodymium disk magnet (Neomax, Japan), rated 2400 Gs at the face surface, was placed noninvasively over the surface of the tumor using a 3D-printed belt. Optical imaging was performed using an FMT 4000 fluorescence tomography imaging system (PerkinElmer, Inc., Waltham, Massachusetts, USA). HeLa tumor-bearing mice were injected intravenously with ICG, and ICG-labeled Fe<sub>3</sub>O<sub>4</sub>-CMSC nanoparticles at a dose of 5 mg/g based on the body weight of the mice, images of the mice were captured 24 h post-injection. At 24 h post-injection, the major organs, i.e., heart, liver, lungs, spleen, and kidneys, along with the tumor were harvested and imaged. The fluorescence images were obtained using an ICG filter (780/845 nm for excitation and emission wavelengths) with an exposure time of 10 s.

#### ***Evaluation of Fe<sub>3</sub>O<sub>4</sub>-CMSC-5FU nanoparticles therapy and photothermal therapy in mouse model***

HeLa tumor-bearing mice were injected intravenously with Fe<sub>3</sub>O<sub>4</sub>-CMSC-5FU nanoparticles at a dose of 5 mg/g and localized with a 13-mm-diameter neodymium disk magnet (Neomax, Japan), 24 h post-injection the tumor was irradiated with a 808 nm NIR laser at a power density of 2 W/cm<sup>2</sup> for 5 and 10 min. Real-time thermal imaging of the tumor was monitored with an FLIR camera thermoIMAGER TIM 160 camera (Micro-Epsilon, USA.). After treatment, the tumor volume was continuously monitored for 14 d.

The tumor dimensions were measured at different time points using a pair of calipers. The tumor volume ( $V$ ) (mm<sup>3</sup>) was determined using the following Eq. (2):

$$V = \frac{\alpha \times \beta^2}{2}, \quad (2)$$

in which  $\alpha$  is the length and  $\beta$  is the width in mm.

The tumor volumes were calculated as  $V/V_0$ , in which  $V_0$  is the initial volume of the tumor before the treatment.

#### **In vivo CT imaging**

HeLa tumor-bearing mice were first anesthetized with intramuscular injection of ketamine + xylazine. After PTT of the Fe<sub>3</sub>O<sub>4</sub>-CMSC-5FU treatment group, CT imaging was obtained on a BioPET/CT 105 (Bioscan, Inc, USA) scanner. The imaging parameters were as follows: voltage, 45 kV; current, 150  $\mu$ A; field of view, 520  $\times$  575; gantry rotation time, 0.5 s.

#### **In vitro MRI**

To acquire the  $T_1$  and  $T_2$  magnetic relaxation for the synthesized Fe<sub>3</sub>O<sub>4</sub>-CMSC-5FU nanoparticles, MRI of the Fe<sub>3</sub>O<sub>4</sub>-CMSC-5FU nanoparticles solutions with different ferrous concentrations of 0, 20, 50, 75, 100 and 200  $\mu$ M were acquired by clinical 1.5 T whole body magnetic resonance (MR) scanner (Signa\* HDxt 1.5T, General Electric Company, USA) at 27 °C. Different spin-echo was applied to measure  $T_1$  images at several differentiation time ( $T_R$ ) such as 100, 1550, 3150, 4750 and 6400 ms with an echo time ( $T_E$ ) of 10 ms, slice thickness of 4 mm, field of view (FOV) of 16  $\times$  12, and matrix

of  $256 \times 198$ . To obtain a spin-echo sequence to measure  $T_2$  images with several echo time ( $T_E$ ) of 10, 40, 75, 110 and 140 ms with a fixed repetition time ( $T_R$ ) of 1600 ms, slice thickness of 4 mm, a field of view (FOV) of  $16 \times 12$ , and matrix of  $256 \times 198$ . The signal intensity was measured from MRI images at each concentration using Dicom Works 1.3.5 software. The signal intensity of the samples from the region of interest was acquired manually. The signal intensity versus  $T_R$  and  $T_E$  was plotted exponentially and fitted using the following equations:

$$I = M_0 \left( 1 - \exp\left(-\frac{T_R}{T_1}\right) \right), \quad (3)$$

$$I = M_0 \left( \exp\left(-\frac{T_E}{T_2}\right) \right), \quad (4)$$

in which,  $I$  = signal intensity and  $M_0$  = constant.

The  $T_1$  and  $T_2$  relaxation parameters, which represent the application of the  $\text{Fe}_3\text{O}_4$ -CMSC-5FU nanoparticles as contrast agents, were calculated from the linear relationship obtained.

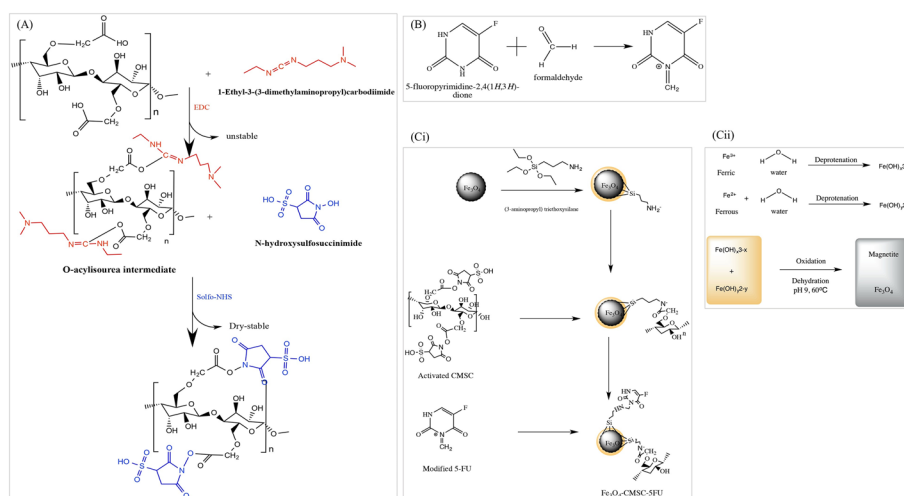
## Results and discussion

Figure 1A shows the effect of the drug-loading and encapsulation efficiency of the  $\text{Fe}_3\text{O}_4$ -CMSC. The CMSC concentration had a significant effect on the drug loading of the nanoparticles. The loading of 5-FU decreased from 85 to 70% as the CMSC concentration increased from 50 to 250 mg. This was owing to the increase of steric hindrance of the polysaccharide, which inhibits the binding of 5-FU to the complex.

The FESEM photographs of  $\text{Fe}_3\text{O}_4$ -NH<sub>2</sub> (Fig. 1B (i)) illustrates the surface morphology of the  $\text{Fe}_3\text{O}_4$ -NH<sub>2</sub> nanoparticles were not agglomerated. The nanoparticles were spherical and had an even size distribution. The FESEM photographs of the  $\text{Fe}_3\text{O}_4$ -5FU show the surface modifications of the nanoparticles in the (Fig. 1B (ii)), which the drug crystals were visible on the rough surface, when compared to the ferrous nanoparticles conjugated with CMSC alone (Fig. 1B (iii)), which exhibited a smooth clumped up surface. The  $\text{Fe}_3\text{O}_4$ -CMSC-5FU surface morphology was similar to the nanoparticles  $\text{Fe}_3\text{O}_4$ -5FU and  $\text{Fe}_3\text{O}_4$ -CMSC samples (Fig. 1B (ii) and (iii)). All the images were obtained at approximately 7-30k times magnification to obtain detailed information about the synthesized nanoparticles. Transmission electron microscopy was used to acquire information on the sizes and shapes of the prepared nanostructures. Figure 1C represents the TEM images of the  $\text{Fe}_3\text{O}_4$ -NH<sub>2</sub> (Fig. 1C (i) & (ii)) and  $\text{Fe}_3\text{O}_4$ -CMSC-5FU particles (Fig. 1C (iii) & (iv)), from which it was inferred that the crystalline particles were coated with a non-crystalline layer of CMSC polymer. The size of the prepared nanoparticles was approximately 20 nm. No aggregates were observed and the  $\text{Fe}_3\text{O}_4$ -NH<sub>2</sub> and  $\text{Fe}_3\text{O}_4$ -CMSC-5FU particles maintained their nanometric size.

## Preparation and optimization of $\text{Fe}_3\text{O}_4$ and $\text{Fe}_3\text{O}_4$ -CMSC-5FU

The formation of an amide bond between carboxylic groups of CMSC and the amine groups of the amino-functionalized  $\text{Fe}_3\text{O}_4$  nanoclusters achieved in the presence of EDC and NHS. A schematic diagram of the reaction is illustrated in Fig. 2A. An



**Fig. 2** **A** Reaction scheme of the formation of CMSC activation using EDC/Sulfo-NHS. **B** Reaction scheme of the formation of 5-FU using formamide. **(Ci)** Reaction scheme for formation of Fe<sub>3</sub>O<sub>4</sub> and **(Cii)** reaction scheme of the formation of Fe<sub>3</sub>O<sub>4</sub>-NH<sub>2</sub> conjugated 5FU stabilized with CMSC

amine-reactive O-acylisourea intermediate compound formed when EDC reacts with a carboxyl group, which is stabilized by NHS, allowing the reaction with the primary amine of the Fe<sub>3</sub>O<sub>4</sub>-NH<sub>2</sub>. The 5-FU was functionally modified using formalin (40% formaldehyde in aqueous) as shown in Fig. 2B.

Figure 2Ci shows the schematic for the formation of black precipitate which is the Fe<sub>3</sub>O<sub>4</sub> nanoparticles. The origin of nanoparticles in the supersaturated reaction medium under optimum conditions begins with a formation of a tiny crystalline nuclei followed by crystal growth (Gupta and Gupta 2005). The prepared Fe<sub>3</sub>O<sub>4</sub> was functionalized with CMSC to provide a stable magnetic nanoparticle and then conjugated with a 5-FU drug to treat cancer cells. The syntheses of the CMSC-coated Fe<sub>3</sub>O<sub>4</sub> particles are shown in Fig. 2Cii. Twenty formulations (F1–F20) with different CMSC concentrations and drug loading were used, and these parameters were crucial to determine the properties of the nanoparticles with 5-FU.

### Structural analysis

To improve the dispersibility of the nanoparticles, the CMSC-conjugated Fe<sub>3</sub>O<sub>4</sub> particles were formed through the reaction of the carboxyl group on CMSC with the amino group on the ferrous magnetic particles. To confirm that CMSC was effectively conjugated to Fe<sub>3</sub>O<sub>4</sub> particles, the existence of a NH<sub>2</sub> group on the Fe<sub>3</sub>O<sub>4</sub> nanoparticles surface was evaluated by determining the functional groups using FTIR (Fig. 3A). The FTIR spectrum of the Fe<sub>3</sub>O<sub>4</sub>-NH<sub>2</sub> nanoparticles showed that Fe<sub>3</sub>O<sub>4</sub> was successfully coated with silica, with the existence of a Si–O–Si peak evident at 1150 cm<sup>-1</sup> (Artopoulou et al. 2016). The characteristic Fe–O–Fe peak of Fe<sub>3</sub>O<sub>4</sub>-NH<sub>2</sub> appeared at 583 cm<sup>-1</sup>. It was inferred that the silica shell was linked to the surface of the magnetic nanoparticles by a Fe–O–Si chemical bond (El-Damrawi et al. 2016). The peaks at 570 and 575 cm<sup>-1</sup> appeared for the bulk Fe<sub>3</sub>O<sub>4</sub> nanoparticles. This blue shift was a result of a decrease in the size of the iron oxide (Xu et al. 2007). The bands at 996 and 1126 cm<sup>-1</sup> confirmed

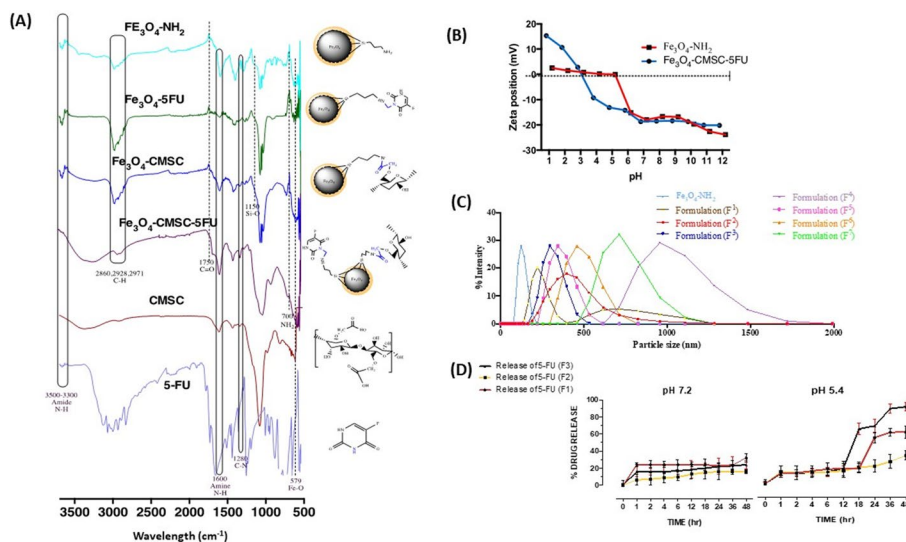


**Fig. 3** **A** FTIR spectra of Fe<sub>3</sub>O<sub>4</sub>-NH<sub>2</sub>, Fe<sub>3</sub>O<sub>4</sub>-5FU, Fe<sub>3</sub>O<sub>4</sub>-CMSC, Fe<sub>3</sub>O<sub>4</sub>-CMSC-5FU, 5-FU, CMSC infrared spectra measured between 600 and 4000 cm<sup>-1</sup>. **B** Zeta potential of Fe<sub>3</sub>O<sub>4</sub>-NH<sub>2</sub> and Fe<sub>3</sub>O<sub>4</sub>-CMSC-5FU particles dispersed in water with different pH. **C** Particle size distribution of various formulation (F1–F7) nanoparticles and Fe<sub>3</sub>O<sub>4</sub>-NH<sub>2</sub>. **D** In vitro percent cumulative release of promising 5-FU formulations (F1, F2 and F3) in pH 5.4 and 7.2 buffer ( $n = 6 \pm \text{s.d.}$ )

that Si–O stretching vibrations were present, which proved the presence of (3-aminopropyl) triethoxysilane (APTES) on the surface of the Fe<sub>3</sub>O<sub>4</sub> nanoparticles. The broad band at 1625 cm<sup>-1</sup> and the split band at 3414 cm<sup>-1</sup> were attributed to the N–H stretching vibration and NH<sub>2</sub> bending mode of free NH<sub>2</sub> groups, respectively (Gautam et al. 2016). The characteristic peaks of Fe<sub>3</sub>O<sub>4</sub>-NH<sub>2</sub> at 3500–3300 cm<sup>-1</sup> corresponding to the  $\nu_{\text{N-H}}$  of the weakened -NH functional group. The above information from the IR spectra verified that the -NH<sub>2</sub> group was successfully introduced on the Fe<sub>3</sub>O<sub>4</sub> particles so that the formation of an amide bond could take place with a carboxyl group from CMSC during the chemical synthesis. To verify this, the characteristic spectrum of Fe<sub>3</sub>O<sub>4</sub>-CMSC was analyzed and the peak at 1700–1500 cm<sup>-1</sup> corresponding to the -COOH group of the CMSC, which would take part in the conjugation with Fe<sub>3</sub>O<sub>4</sub>-NH<sub>2</sub> through an amide bond, was monitored. The conjugation of 5-FU to Fe<sub>3</sub>O<sub>4</sub>-NH<sub>2</sub> was confirmed with the presence of the stretch at 1690–1630 cm<sup>-1</sup> corresponding to an amine bond. The dark field scanning transmission electron microscopy (STEM) images (not shown) of Fe<sub>3</sub>O<sub>4</sub>-NH<sub>2</sub> and Fe<sub>3</sub>O<sub>4</sub>-CMSC-5FU confirmed that Fe<sub>3</sub>O<sub>4</sub> nanocrystals were present. The elemental mapping of C, O, Si and Fe by energy-dispersive X-ray spectroscopy (STEM-EDX—not shown) on Fe<sub>3</sub>O<sub>4</sub>-NH<sub>2</sub> confirmed the presence of a silica coating on the Fe<sub>3</sub>O<sub>4</sub> nanoparticles. This was also confirmed by FTIR (Fig. 3A). The EDX spectrum of Fe<sub>3</sub>O<sub>4</sub>-CMSC-5FU showed elemental mapping of C, O, F, Na, and Fe, which proved the presence of CMSC from Na, O and C, 5-FU from F (fluorine) and Fe<sub>3</sub>O<sub>4</sub> nanoparticles from Fe, and Si, which were homogeneously distributed in the nanoparticles.

To verify the effects of pH on nanoparticles, the polyionic charges were measured. The zeta potential for Fe<sub>3</sub>O<sub>4</sub>-NH<sub>2</sub> particles and Fe<sub>3</sub>O<sub>4</sub>-CMSC-5FU (100 µg/mL) were performed at different pHs (1–12) (Fig. 3B). The Fe<sub>3</sub>O<sub>4</sub>-NH<sub>2</sub> was found to be stable from pH 1.0 to 6.0, where it is a neutral electrophoretic charge. The isoelectric point (pI), is the

pH at which a particular molecule carries zero net electrical charges (Ulaganathan et al. 2017). However, the isoelectric point (pI) of  $\text{Fe}_3\text{O}_4\text{-NH}_2$  shifted from 5.2 to 3.1 due to surface modifications in  $\text{Fe}_3\text{O}_4\text{-CMSC-5FU}$ .

The size distribution of nanoparticles F1–F7 was evaluated and presented in Fig. 3C. As the CMSC concentration increased, the particle size increased from 200 to 1500 nm and had a broad distribution, which confirmed that different size nanoparticles were present in the formulation. This could be because more surface coating occurred with increasing polymer concentration. This trend was similar to the increase of the 5-FU concentration (F6–F7). It has been suggested that size of the nanoparticles play a major role in their adhesion to and interaction with biological cells (Verma and Stellacci 2010). Particles that are approximately 100–200 nm can be internalized by endocytosis and have better interfacial interactions with the cell membrane, whereas larger particles would be taken up by fluid-phase pinocytosis (Garnacho 2016). Therefore, the small size nanoparticles could improve the efficacy of the nanoparticle-based drug delivery system. F1, F2 and F3 were further evaluated because the nanoparticles fall in narrow size distribution and also provide the strongest magnetization of the  $\text{Fe}_3\text{O}_4$  nanoparticles.

The 5-FU release profiles from formulations F1–F3 in pH 5.4 and 7.2 buffer solution at 37 °C are shown in Fig. 3D. As shown in Fig. 3D, a similar release trend was observed for all the tested systems, in which all samples showed an initial fast release in the first hour at pH 5.4 followed by a slow and continuous release. At pH 5.4, only 20% 5-FU was released within 18 h, which quickly increased to 70% after 48 h for F1 and 100% for F3. When the pH of the solution was 7.2, an insignificant amount of drug was released from all the formulation. The release of the drug within the first hour mainly resulted from the surface-bound 5-FU molecules. Moreover, the second stage was a relatively slow release up to 48 h, which was attributed to the cleavage of the amide bond formed between the drug and the nanoparticle. The formation of the complex was owing to formation of amine bonding, and the pH-dependent release from the complex was attributed to the cleavage of the amine bond between the complex and 5-FU. At pH 7.2, hydrolysis did not occur until 48 h, whereas at pH 5.4 the hydrolysis occurred after 12 h. Thus, the release of 5-FU was not observed at pH 7.2. In an acidic environment, the tautomeric conversion of 5-FU can play a fundamental role in the hydrolysis and release of the drug. A lower pH can cause a high degree of protonation of 5-FU. In other words, at pH 5.4, there was complete hydrolysis of the bond between 5-FU and nanocomplex. The drug release profile was analyzed at pH 7.2 and 5.4. The amine bond was hydrolyzed at acidic pH, and there was no or minimal drug release at pH 7.2. At pH 5.4, 100% of the drug was released within 48 h in all formulations, whereas 0–20% of the drug was released at pH 7.2. This release profile is more feasible for cancer treatment and achieves more target specificity owing to pH response (Fig. 3D).

Furthermore, increasing CMSC concentration also affected the magnetization of the  $\text{Fe}_3\text{O}_4$  nanoparticles. This is evident in Fig. 4A, which shows that that increasing the concentration of CMSC (100–200 mg) in the formulation of F2–F4 reduced the magnetization from 26.35 to 5.89 emu/g (Chen et al. 2007). A hysteresis loop for the nanoparticles was observed, which clearly proved that  $\text{Fe}_3\text{O}_4\text{-CMSC-5FU}$  exhibited superparamagnetic behavior. This indicated that the optimum CMSC concentration used for synthesis was 50 mg (F1) to achieve the highest drug loading (Hamidi et al. 2013). At the same

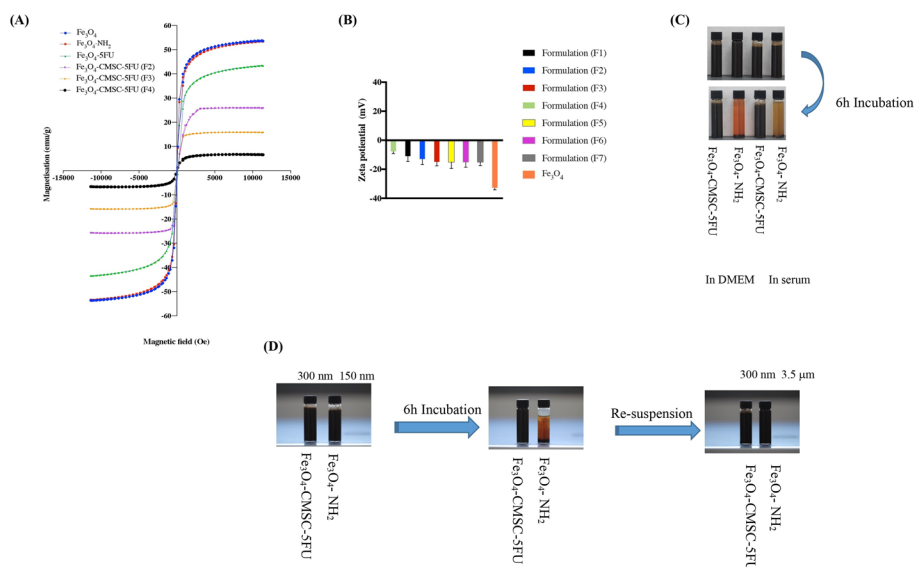


**Fig. 4** **A** Dependence of the applied magnetic field on the saturation magnetization of  $\text{Fe}_3\text{O}_4$ ,  $\text{Fe}_3\text{O}_4\text{-NH}_2$ ,  $\text{Fe}_3\text{O}_4\text{-5FU}$ ,  $\text{Fe}_3\text{O}_4\text{-CMSC-5FU}$  (F2, F3, F4) nanoparticles. **B** Zeta potential of different  $\text{Fe}_3\text{O}_4\text{-CMSC-5FU}$  formulations and  $\text{Fe}_3\text{O}_4$  in PBS at pH 7. **C** Stability of  $\text{Fe}_3\text{O}_4\text{-NH}_2$ ,  $\text{Fe}_3\text{O}_4\text{-CMSC-5FU}$  in DMEM and serum. **D** Stability of  $\text{Fe}_3\text{O}_4\text{-NH}_2$ ,  $\text{Fe}_3\text{O}_4\text{-CMSC-5FU}$  in PBS after 6 h incubation

time, as the drug loading increased to the maximum value, the entrapment efficiency decreased. This was because the amount of drug that could conjugate to the nanoparticles reached a saturation point, and a higher proportion of the drug was lost in the liquid medium during conjugation. Therefore, the maximum loading of the 5-FU drug on 1200 mg of  $\text{Fe}_3\text{O}_4\text{-CMSC-5FU}$  was 250 mg. This helped us to narrow our investigation to the most favorable formulations F1–F7.

To verify the effect of the pH on the nanoparticles, the polyionic charges of F1–F7 were measured (Fig. 4B) at pH 7. All the formulations showed a negative charge. At pH 7, the  $-\text{OCH}_2\text{COOH}$  groups on the CMSC chains were negatively charged owing to deprotonation of the carboxylic acid groups (dissociation of  $\text{Na}^+$ ).

The modification of the nanoparticles with CMSC is crucial, because it can be used to increase the surface charge of the nanoparticles to stabilize the suspensions or to initiate flocculation by (a) neutralizing the surface charge and (b) acting as a bridge between particles. The zeta potential of  $\text{Fe}_3\text{O}_4$  particles was measured as  $-38$  mV, as shown in Fig. 4B, and the zeta potential of the F1–F7 nanoparticles obtained after the modification with CMSC was measured as  $-18$  to  $-20$  mV. The zeta potential measurement results indicated that the negative charge of CMSC decreased the zeta charge of the  $\text{Fe}_3\text{O}_4$  nanoparticles by modification with the new functional group. The reason that the  $\text{Fe}_3\text{O}_4$  nanoparticles did not have a zero charge was because it is not possible to have a positive charge for every carboxylic acid groups in the structure (not 100% modification). However, the increased of zeta potential from  $-38$  to  $-20$  mV demonstrated that the positive charges were successfully generated. As shown in Fig. 4B, the zeta potential decreased with increasing ionic strength owing to the increasing concentration of CMSC (F2, F3 and F5). This also affected the magnetization of the  $\text{Fe}_3\text{O}_4$  nanoparticles. In Fig. 4A, it was observed that increasing the concentration of CMSC also reduced the

magnetization from 26.35 to 5.89 emu/g (Chen et al. 2007). A hysteresis loop for the nanoparticles was observed, which proved that Fe<sub>3</sub>O<sub>4</sub>-CMSC-5FU displayed ferromagnetic behavior. The magnetization of the nanoparticles is crucial as the magnetic field of the nanoparticles needs to be strong enough to be pulled towards the target side, at which the rare earth magnets are focused. On the other hand, the zeta potential of F4 was found to be lower than F1. This could be because of the inhibition of intermolecular aggregation owing to increasing electric repulsion resulting in greater stability. The aggregation of the nanoparticles in solution could be related to the charge of the complex, in which different charges are present and will induce different behavior. Generally, when all the particles have a large negative charge, they will repel each other, and the dispersion is stable. On the other hand, when the particles have a low negative charge as in F4, there is no sufficient force to prevent the nanoparticles from aggregating.

The stability of nanoparticles were evaluated in phosphate buffer, DMEM, and fetal bovine serum. According to Fig. 4C and D, Fe<sub>3</sub>O<sub>4</sub>-CMSC-5FU appeared to be dispersed after 6 h in phosphate buffer, DMEM, and fetal bovine serum but was not the same for Fe<sub>3</sub>O<sub>4</sub>-NH<sub>2</sub> as it sediments at the bottom of the bottle. However, after the re-suspension of both samples in phosphate buffer, it can be seen particle size increased from 100 to 3500 nm. Although the stability of Fe<sub>3</sub>O<sub>4</sub> nanoparticles has been widely studied, it is also true that they tend to agglomerate when they are dispersed in PBS or serum. This could be because of the change in the surface charge of the nanoparticles. When they are considered for the application as therapeutic agents, it is vital to prevent agglomeration as these nanoparticles tend to possibly block the blood capillaries in vivo (Mahmoudi et al. 2011). Carboxymethylcellulose modification will stabilize the nanoparticles in a physiological environment. The stability of these nanoparticles Fe<sub>3</sub>O<sub>4</sub>-NH<sub>2</sub> and Fe<sub>3</sub>O<sub>4</sub>-CMSC-5FU were examined in PBS, DMEM, and serum. From Figure, we can prove that Fe<sub>3</sub>O<sub>4</sub>-NH<sub>2</sub> were agglomerating from settling at the bottom when dispersed in PBS, DMEM and serum after 6 h incubation whereas, Fe<sub>3</sub>O<sub>4</sub>-CMSC-5FU did not show any agglomeration and stayed dispersed until 6 h. When Fe<sub>3</sub>O<sub>4</sub> dispersion was re-suspended using pipette the opalescence was not achieved and particle size increased from 100 to 3500 nm. This increase in the particle size was not observed in the Fe<sub>3</sub>O<sub>4</sub>-CMSC-5FU thus proving CMSC modification is an effective tactic to improve the stability and compatibility of Fe<sub>3</sub>O<sub>4</sub>-NH<sub>2</sub>.

The photothermal effect from the irradiation of Fe<sub>3</sub>O<sub>4</sub>-NH<sub>2</sub> and Fe<sub>3</sub>O<sub>4</sub>-CMSC-5FU with a NIR laser (808 nm) at a power density of 600 mW/cm<sup>2</sup> was evaluated by exposing the magnetic nanoparticle suspensions (1 mL) of various concentrations (30, 75, 175 and 350 mg mL<sup>-1</sup>) (Fig. 5A). The temperature of the suspension was monitored in 60 s intervals for a total of 15 min with a thermocouple immersed in the sample solution. To observe the photothermal effect, Fe<sub>3</sub>O<sub>4</sub>-NH<sub>2</sub> suspensions with different concentrations were irradiated with a 808 nm laser at a power density of 600 mW/cm<sup>2</sup> with PBS as a control (Fig. 5B). A remarkable temperature increases to 92.2°C was observed at a concentration of 350 mg mL<sup>-1</sup> under irradiation for 15 min, whereas no obvious temperature increase was observed when the PBS control was irradiated under the same conditions.

A similar study on the effects of silica encapsulation and SPION clustering on both magnetic hyperthermia and photothermic resulted that SPION clustering reduced

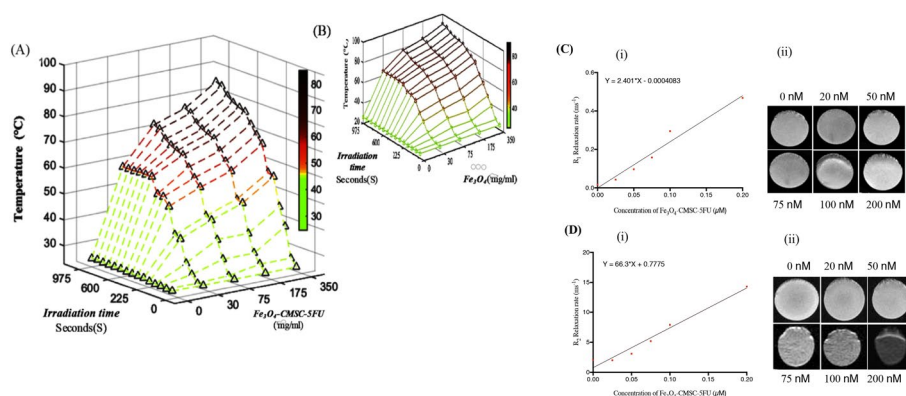


**Fig. 5** A Evaluation of the photothermal effect. The heating curves of **A**  $\text{Fe}_3\text{O}_4$ -CMSC-5FU (30, 75, 175 and 350  $\text{mg mL}^{-1}$ ) **B**  $\text{Fe}_3\text{O}_4$  (30, 75, 175 and 350  $\text{mg mL}^{-1}$ ) as a function of irradiation, time under 808 nm laser irradiation at a power density of  $600 \text{ mW/cm}^2$ . **C** (i)  $T_1$  relaxation rate plotted as a function of  $\text{Fe}_3\text{O}_4$ -CMSC-5FU concentration and  $1/T_1 \text{ s}^{-1}$ , (ii)  $T_1$ -weighted MRI images (1.5T, spin-echo sequence: repetition time  $\text{TR} = 1550 \text{ ms}$ , echo time  $\text{TE} = 10 \text{ ms}$ ) of  $\text{Fe}_3\text{O}_4$ -CMSC-5FU nanoparticles at various concentrations and  $1/T_2 \text{ s}^{-1}$  at  $27^\circ\text{C}$ . **D** (i)  $T_2$  relaxation rate plotted as a function of  $\text{Fe}_3\text{O}_4$ -CMSC-5FU concentration (ii)  $T_2$ -weighted MRI images (1.5T, spin-echo sequence: repetition time  $\text{TR} = 1600 \text{ ms}$ , echo time  $\text{TE} = 110 \text{ ms}$ ) of  $\text{Fe}_3\text{O}_4$ -CMSC-5FU nanoparticles at various concentration at  $27^\circ\text{C}$

heat generation in magnetic hyperthermia, the silica shell improved SPION heating in photothermic (Nemec et al. 2020). Another research delved into the photothermal effectiveness of superparamagnetic iron oxide nanoparticles (SPIONs), specifically  $\text{Fe}_3\text{O}_4$ , in conjunction with various nanomaterials such as graphene oxide, polydopamine, and Aurum (Au). Upon exposure to 808 nm infrared laser stimulation, this combination demonstrated a notable decrease in the viability of HepG2 liver cancer cells, KB nasopharyngeal cancer cells, and MCF-7 breast cancer cells at varying efficacy levels, achieving lethality rates ranging from 30 to 80% in vitro. (El-Sherbiny et al. 2020).

### Crystallographic analysis

X-ray diffraction studies of the prepared nanoparticle formulations (F1 and F3) were carried out to check the physical nature of the particles. Peaks of  $\text{Fe}(\text{OH})_3$  ( $2\theta = 26.380^\circ$ ), goethite ( $2\theta = 21.220^\circ$ ) and hematite ( $2\theta = 33.150^\circ$ ) were not observed. A broad weak band ( $2\theta = 17\text{--}26^\circ$ ) was observed in the XRD pattern of  $\text{Fe}_3\text{O}_4\text{-NH}_2$  (Zhang et al., 2008a), which was attributed to the amorphous silica shell formed surrounding the magnetic core. Comparing the  $\text{Fe}_3\text{O}_4$ -CMSC-5FU nanoparticles with the 5-FU drug, CMSC,  $\text{Fe}_3\text{O}_4\text{-NH}_2$  and  $\text{Fe}_3\text{O}_4$ -CMSC as a control, it was observed that  $\text{Fe}_3\text{O}_4$ -CMSC-5FU was much more amorphous compared with the 5-FU drug alone. The amorphous nature of the  $\text{Fe}_3\text{O}_4$ -CMSC-5FU was attributed to the crosslinking mechanism between the reactive residual functional groups of CMSC, which formed a coating around the nanoparticles and reduced the crystalline nature of the drug. Additional file 1 Fig. S1 shows the XRD pattern of 5-FU and 5-FU-loaded nanoparticles, which indicated the successful conjugation of CMSC and 5-FU to the  $\text{Fe}_3\text{O}_4\text{-NH}_2$  nanoparticles. For the free 5-FU, the X-ray diffractograms exhibited an intense peak at  $2\theta$  near  $28^\circ$  owing to its crystalline nature (Additional file 1: Fig. S1), whereas from  $\text{Fe}_3\text{O}_4\text{-NH}_2$ ,  $\text{Fe}_3\text{O}_4$ -CMSC,  $\text{Fe}_3\text{O}_4$ -5FU,

Fe<sub>3</sub>O<sub>4</sub>-CMSC-5FU (F1, F3), only the nanoparticles conjugated with 5-FU showed a similar peak and other samples did not exhibit a characteristic peak of 5-FU.

#### Evaluation of Fe<sub>3</sub>O<sub>4</sub>-CMSC-5FU as an MRI contrasting agent

The  $1/T_1$  and  $1/T_2$  plots versus concentration of Fe<sub>3</sub>O<sub>4</sub>-CMSC-5FU nanoparticles (Fig. 5C and D) were used to derive  $r_1$  relaxation time and  $r_2$  relaxation time as 2.4 and 66 mM<sup>-1</sup> s<sup>-1</sup>, respectively. However, the efficiency of the Fe<sub>3</sub>O<sub>4</sub>-CMSC-5FU nanoparticles as a contrasting agent was determined by acquiring the ratio between the transverse and longitudinal relaxivity ( $r_2/r_1$ ) (Arsalani et al. 2010). The ratio of the Fe<sub>3</sub>O<sub>4</sub>-CMSC-5FU nanoparticles was determined as 27.5, which was much higher than commercially available ferucarbotran (Resovist, Bayer Healthcare) (Corot et al. 2006). The Fe<sub>3</sub>O<sub>4</sub> nanoparticles can be used as an excellent T<sub>2</sub> (negative enhancement) contrast agent in MRI, and because CMSC exhibits high biocompatibility, the Fe<sub>3</sub>O<sub>4</sub>-CMSC-5FU nanoparticles were investigated as an MR signal-enhancing agent. This was studied by acquiring the T<sub>2</sub>-weighted MR images of different concentrations of Fe<sub>3</sub>O<sub>4</sub>-CMSC-5FU nanoparticles. As shown in Fig. 5D (ii), T<sub>2</sub>-weighted MR images of various concentration of Fe<sub>3</sub>O<sub>4</sub>-CMSC-5FU nanoparticles in PBS (a spin-echo technique with TR = 4200 and TE = 91 ms) was measured. The MR signal intensity related to T<sub>2</sub> relaxation time in the T<sub>2</sub>-weighted images of Fe<sub>3</sub>O<sub>4</sub>-CMSC-5FU nanoparticles were not similar at different concentrations. It was observed that with an increase in the concentration of Fe<sub>3</sub>O<sub>4</sub>-CMSC-5FU nanoparticles, the MR signals were significantly increased. The T<sub>2</sub>-weighted images negative signals were brighter and the positive signal was darker. The transfer of energy between the protons in the water molecules causes the T<sub>2</sub> relaxation processes. The T<sub>2</sub> shortening occurs when Fe<sub>3</sub>O<sub>4</sub>-CMSC-5FU nanoparticles create non-uniformity (inhomogeneity) in the magnetic field, causing changes in the microenvironment. The correlation coefficient of 0.0065 suggest linear relationship between the concentration of nanoparticles (NPs) and the  $r_2$  relaxation values (Freedman 1990). This indicated that Fe<sub>3</sub>O<sub>4</sub>-CMSC-5FU nanoparticles can be used as a T<sub>2</sub> contrasting agent.

#### Cellular uptake

The HeLa cells and HEK 293 cells displayed very different result when exposed to Fe<sub>3</sub>O<sub>4</sub> and Fe<sub>3</sub>O<sub>4</sub>-CMSC-5FU nanoparticles. The cell viability and morphology of the HeLa cells were changed dramatically when exposed to Fe<sub>3</sub>O<sub>4</sub>-CMSC-5FU when compared with the HEK 293 cells. This could be because the HeLa cells are cancerous, and the HEK cells are non-cancer cell lines. The HeLa cells were observed to shrink in size and eventually undergo apoptosis with increasing concentration of the nanoparticles, whereas the HEK cells did not show as much response to the nanoparticles and exhibited a low cell uptake of the nanoparticles (Murgia et al. 2010). Figure 6A(i) clearly shows that the Fe<sub>3</sub>O<sub>4</sub> nanoparticles did not cause any toxicity to HeLa cells, whereas Fe<sub>3</sub>O<sub>4</sub>-CMSC-5FU at a concentration of 1 g/mL caused cell apoptosis, whereas similar concentrations did not cause any cell death in HEK cells (Fig. 6A(ii)). It was also observed that cellular uptake was much lower in HEK cells owing to the cell morphology of cancer and non-cancer cells. Increasing the concentration of Fe<sub>3</sub>O<sub>4</sub>-CMSC-5FU caused more cell death resulting in less cell count in the HeLa cells and increased cell uptake in the HEK cells. There was a

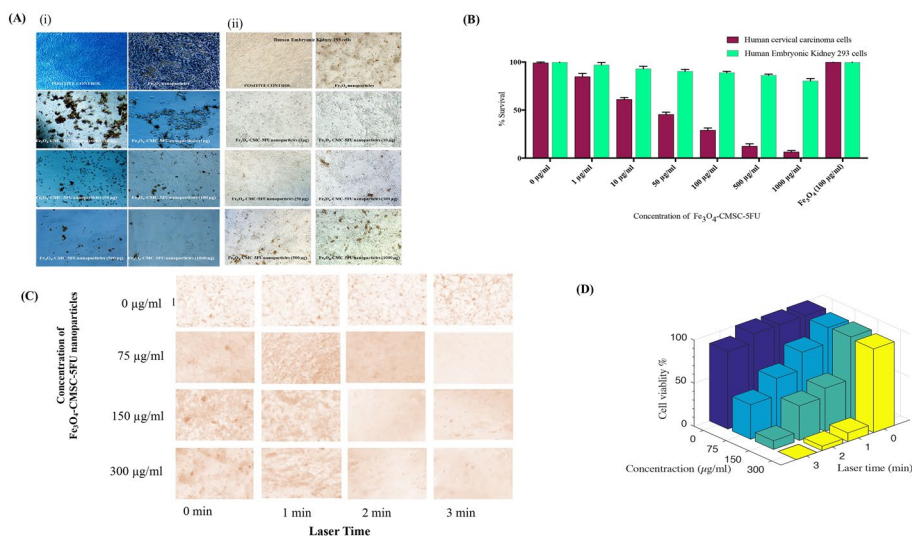


**Fig. 6** **A** (i) Cell uptake and toxicity studies of Fe<sub>3</sub>O<sub>4</sub>-CMSC-5FU complexes on human cervical carcinoma cells. (ii) Cell uptake and toxicity studies of Fe<sub>3</sub>O<sub>4</sub>-CMSC-5FU complexes on Human Embryonic Kidney 293 cells. **B** Cytotoxicity studies of Fe<sub>3</sub>O<sub>4</sub> and Fe<sub>3</sub>O<sub>4</sub>-CMSC-5FU complexes on human cervical carcinoma cells and Human Embryonic Kidney 293 cells (n = 3 ± s.d.). **C** Photothermal studies of Fe<sub>3</sub>O<sub>4</sub>-CMSC-5FU complexes on human cervical carcinoma cells. **D** Cytotoxicity studies of Fe<sub>3</sub>O<sub>4</sub>-CMSC-5FU complexes along with photothermal therapy on human cervical carcinoma cells

slight change in the cell morphology of the HEK cells with increasing Fe<sub>3</sub>O<sub>4</sub>-CMSC-5FU concentration, but this did not cause rapid cell death, in contrast to that with HeLa cells.

### Cytotoxicity of Fe<sub>3</sub>O<sub>4</sub>-CMSC-5FU

HeLa cells and HEK cells were exposed to Fe<sub>3</sub>O<sub>4</sub> and Fe<sub>3</sub>O<sub>4</sub>-CMSC-5FU nanoparticles with a viable cell count. The Fe<sub>3</sub>O<sub>4</sub> nanoparticles with a concentration of 100 µg/mL did not exhibit any cell toxicity in both carcinogenic and non-carcinogenic cell lines. In contrast, the Fe<sub>3</sub>O<sub>4</sub>-CMSC-5FU nanoparticles showed cell toxicity in HeLa cells (Fig. 6B) and were nontoxic to HEK cells. The increase in concentration increased the cell death in HeLa cells and had no effect on the HEK cell lines. The cell toxicity might be owing to the presence of the cytotoxic drug in the formulation and release of the drug depending on the pH of the environment. The non-treated control cells were grown with no sign of toxicity. It has been reported that different cell lines may exhibit different toxicity, which depends on the particle size and surface charge of the nanoparticle.

### Photothermal destruction of cancer cells in vitro

To evaluate the photothermal toxicity of the nanoparticles in vitro, HeLa cells were used as cancer cell models. Cells were incubated with different concentrations of Fe<sub>3</sub>O<sub>4</sub>-CMSC-5FU (F3) nanoparticles (75, 150 and 300 µg/mL). Then the cells were irradiated using a 808 nm laser at a power density of 2 W/cm<sup>2</sup> for 0–3 min. It was evident that the photothermal effect induced by NIR laser irradiation enhanced the ability of Fe<sub>3</sub>O<sub>4</sub>-CMSC-5FU to destroy cancer cells efficiently (Fig. 6C). There was a significant change in the cell morphology when compared to the control, and cell death was evident with an increase in irradiation time and concentration of Fe<sub>3</sub>O<sub>4</sub>-CMSC-5FU (F3) nanoparticles.

Quantitative evaluation of cell death owing to treatment with Fe<sub>3</sub>O<sub>4</sub>-CMSC-5FU combined with PTT showed that over 90% of the HeLa cells did not survive within 3 min of irradiation using an 808-nm laser. However, no significant cancer cell death was observed when the cells were irradiated without the presence of nanoparticles (Fig. 6D). Thus, the cell death was owing to the combined treatment with Fe<sub>3</sub>O<sub>4</sub>-CMSC-5FU (F3) nanoparticles and irradiation with an 808-nm laser.

The Fe<sub>3</sub>O<sub>4</sub> nanoparticles exhibited a similar photothermal effect, which could increase the temperature of the solution by 15°C more than the Fe<sub>3</sub>O<sub>4</sub>-CMSC-5FU (F3) nanocomplex. This proved that Fe<sub>3</sub>O<sub>4</sub> can consume NIR light and transfer it to heat energy very efficiently. The Fe<sub>3</sub>O<sub>4</sub>-CMSC-5FU was shown to enter the cancer cell effectively, and NIR absorption caused molecular oscillation, which led to efficient heat production around the surrounding environment. Because the nanoparticles exhibited a selectivity for cancer cells, they effectively acted as a novel thermal ablation agent for photothermal destruction of cancer cells. When a PTT study was performed on Fe<sub>3</sub>O<sub>4</sub>-CMSC-5FU (300 µg/mL), up-taken cancer cells were destroyed completely within 3 min of irradiation with a 808 nm laser with a power density of 2 W/cm<sup>2</sup> (Fig. 6D).

### **In vivo behavior of Fe<sub>3</sub>O<sub>4</sub>-CMSC-5FU nanoparticles**

#### ***Photothermal ablation of tumor***

The combination of Fe<sub>3</sub>O<sub>4</sub>-CMSC-5FU nanoparticles and near-infrared light (808 nm), which provided thermal therapy to induce thermal ablation in tumor tissues, was effective for cancer therapy. The labeled groups are (i) group treated with Fe<sub>3</sub>O<sub>4</sub>-CMSC-5FU ( $n=5$ ) and laser therapy, (ii) group treated with 100 mg/kg Fe<sub>3</sub>O<sub>4</sub>-CMSC-5FU and no laser therapy ( $n=5$ ), (iii) group treated with only laser therapy ( $n=5$ ), (iv) control group ( $n=5$ ) with no Fe<sub>3</sub>O<sub>4</sub>-CMSC-5FU and no laser therapy. To investigate the hyperthermic potential of the Fe<sub>3</sub>O<sub>4</sub>-CMSC-5FU nanoparticles in vivo, the increase in temperature at the tumor site was monitored by an infrared thermal camera during the irradiation. Figure 7A shows that the temperature increased tremendously up to 55.3 °C and 42.7 °C for the treatment groups (i and iii), respectively, at the center of tumor site for the combined treatment with Fe<sub>3</sub>O<sub>4</sub>-CMSC-5FU nanoparticles and the NIR laser. The tumor that had accumulated Fe<sub>3</sub>O<sub>4</sub>-CMSC-5FU nanoparticles showed a more significant increase in temperature than the tumor that was only irradiated with a NIR laser under identical conditions. The temperature of the tumor that was only treated with NIR laser reached the highest temperature of 42.7 °C at the irradiation center of the tumor for tumor-bearing no nanoparticles (treatment group iii). The average temperature of the tumor administered with the Fe<sub>3</sub>O<sub>4</sub>-CMSC-5FU nanoparticles (i and ii) increased rapidly from 28.2 °C to 49.0 °C after irradiation, which was sufficient for the thermal ablation of the cancer cells. Moreover, the temperature increase was rapid in the first 4 min and then slowed down. In contrast, the average temperature of the tumor for the group of mice that was not administered nanoparticles (iii and iv) only reached 37.9 °C after irradiation. This result suggests that Fe<sub>3</sub>O<sub>4</sub>-CMSC-5FU is ideal for cancer treatment by PTT. The treatment with only NIR laser showed no change in the average temperature at the tumor region in Fig. 7A.

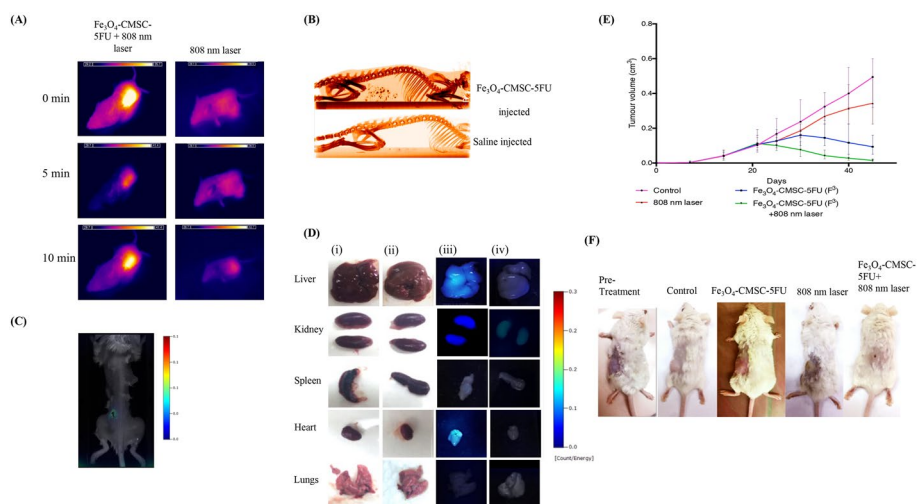


**Fig. 7** **A** Graphical scan of thermal fingerprint of mice treated with  $\text{Fe}_3\text{O}_4$ -CMSC-5FU nanoparticles irradiated with 808 nm laser and only with NIR laser. **B** In vivo CT maximum intensity projection of sagittal images of the tumor-bearing mouse with and without treatment using  $\text{Fe}_3\text{O}_4$ -CMSC-5FU + 808 nm laser. **C** Bio-distribution of  $\text{Fe}_3\text{O}_4$ -CMSC-ICG in mouse model BALB/c. **D** Bio-distribution of ICG (i & iii) and  $\text{Fe}_3\text{O}_4$ -CMSC-ICG (ii & iv) in vital organs. **E** Relative tumor volumes of mice ( $n = 5 \pm \text{s.d.}$ ) treated with  $\text{Fe}_3\text{O}_4$ -CMSC-5FU, 808 nm laser,  $\text{Fe}_3\text{O}_4$ -CMSC-5FU + 808 nm laser. **F** Photographs of mice treated with  $\text{Fe}_3\text{O}_4$ -CMSC-5FU, 808 nm laser,  $\text{Fe}_3\text{O}_4$ -CMSC-5FU with 808 nm laser after 14 days

### CT imaging of mice under magnetic targeting

To confirm that these therapeutic effects were influenced by the particle distribution, the mice were examined by X-ray CT imaging. Figure 7B shows the maximum intensity projection and volume renders of the control mice and  $\text{Fe}_3\text{O}_4$ -CMSC-5FU + 808 nm laser-treated mice. The sagittal view in Fig. 7B confirmed that  $\text{Fe}_3\text{O}_4$ -CMSC-5FU nanoparticles were only present in the tumor site and not dispersed in other sites. In contrast, no intensity projections were observed in the saline injected mice.

These results demonstrated that  $\text{Fe}_3\text{O}_4$ -CMSC-5FU can be used for simultaneous X-ray CT imaging and NIR PTT of tumors. Combining the advantage of deep tissue spatial penetration without tissue damage by CT imaging and the minimal attenuation of the energy and undesirable heating of healthy tissue of PTT, the higher X-ray attenuation coefficient of  $\text{Fe}_3\text{O}_4$ -CMSC-5FU enables it to be used as a CT contrast agent for sensitive CT imaging of tumors. Furthermore, with a high-intensity absorption in the NIR region, the developed  $\text{Fe}_3\text{O}_4$ -CMSC-5FU exhibited high photothermal conversion, amenable for photothermal ablation of cancer cells in vitro and in vivo.

The in vivo behavior of the  $\text{Fe}_3\text{O}_4$ -CMSC-5FU nanoparticles was then investigated using  $\text{Fe}_3\text{O}_4$ -ICG labeled nanoparticles. ICG, a commonly used fluorescent dye, was used to label the  $\text{Fe}_3\text{O}_4$ -NH<sub>2</sub> nanoparticles, which were then used to make  $\text{Fe}_3\text{O}_4$ -CMSC-ICG nanoparticles. After 12 h and 24 h post-intravenous (I.V.) injection with pure ICG and  $\text{Fe}_3\text{O}_4$ -CMSC-ICG, the BALB/c mice were imaged using an FMT 4000 fluorescence tomography imaging system (PerkinElmer, Inc., Waltham, Massachusetts, U.S.).

As shown in Fig. 7C,  $\text{Fe}_3\text{O}_4$ -CMSC-ICG was accumulated at the tumor site over time, with a significant uptake of particles observed in the tumor at 24 h post-injection. However, free ICG was distributed throughout the body of the mice and was difficult

to accumulate in the tumor. This suggested that the fluorescent signals observed at the tumor site were owing to  $\text{Fe}_3\text{O}_4$ -CMSC-ICG and not from free ICG or detached ICG.

The biodistribution of ICG and  $\text{Fe}_3\text{O}_4$ -CMSC-ICG was further evaluated by *in vivo* imaging of the major internal organs of killed mice 24 h post-injection. The fluorescent images of the dissected internal organs and tumor are shown in Fig. 7D (i–iv), which confirmed that the  $\text{Fe}_3\text{O}_4$ -CMSC-ICG nanoparticles could be more efficiently targeted to the tumor site than ICG by itself. The  $\text{Fe}_3\text{O}_4$ -CMSC-ICG nanoparticles could efficiently decrease the distribution of ICG to major organs such as the liver, lung, spleen and heart. The fluorescence intensity of the tumor from  $\text{Fe}_3\text{O}_4$ -CMSC-ICG was much higher than free ICG owing to localization. These results confirmed that PTT should be executed 24 h post-administration.

The biodistribution of the ICG-labeled nanoparticles proves the magnetic targeting ability and localization in the tumor. Compared to free ICG, which was distributed throughout the mice body including vital internal organs (Fig. 7D), the  $\text{Fe}_3\text{O}_4$ -CMSC-ICG nanoparticles were localized using an external magnetic field.

#### **Tumor volume measurement in mouse model BALB/c treated with $\text{Fe}_3\text{O}_4$ -CMSC-5FU using 808 nm laser**

Mice were investigated for *in vivo* PTT and cancer treatment. The heat-inducing ability of the  $\text{Fe}_3\text{O}_4$ -CMSC-5FU nanoparticles used for the treatment was evaluated. The treatment groups  $\text{Fe}_3\text{O}_4$ -CMSC-5FU with 808 nm laser (treatment group i) and only 808 nm laser treatment (group iii) were irradiated by 808 nm laser at a power of  $2 \text{ W/cm}^2$  for 15 min. The mice were killed after 2 weeks with no additional treatment. The temperature of the outside tissue of the tumor xenograft increased to  $49.4 \text{ }^\circ\text{C} \pm 3.9 \text{ }^\circ\text{C}$  during NIR irradiation for 10 min in the treatment group (i) and  $38 \text{ }^\circ\text{C} \pm 2.7 \text{ }^\circ\text{C}$  for treatment group (iii). In the control group, the tumor continued to grow and was bigger than those in the treatment groups after the same period (Fig. 7E). The change in the NIR irradiation temperature was reflected in the total tumor volume of each group. The volume of the tumors excised from the mice treated with  $\text{Fe}_3\text{O}_4$ -CMSC-5FU were smaller than the control and 808 nm laser treatment group. However, the combination of  $\text{Fe}_3\text{O}_4$ -CMSC-5FU with 808 nm laser treatment showed a black scar two days after treatment and a significant reduction in the tumor size. Figure 7F shows representative photographic images of the mice after various treatments. When irradiated only by a NIR laser, the tumor size showed no reduced growth when compared to the control.

#### **Conclusions**

$\text{Fe}_3\text{O}_4$ - $\text{NH}_2$  nanoparticles were successfully conjugated with carboxymethyl sagocelulose (CMSC) to obtain PBS-stable nanoparticles. The CMSC surface modification increased the negative charge of  $\text{Fe}_3\text{O}_4$ , allowing them to accumulate more efficiently in a tumor. The PTT was based on the absorption of light in the NIR wavelength range by the nanoparticles; a higher concentration of  $\text{Fe}_3\text{O}_4$ -CMSC-5FU resulted in an increase in absorption and produces more heat. The modification with CMSC was an effective method for improving the stability and compatibility of  $\text{Fe}_3\text{O}_4$ - $\text{NH}_2$  as it prevented the agglomeration of the nanoparticles in PBS, DMEM and serum after 6 h incubation.

A magnetization curve of the hysteresis loop for the  $\text{Fe}_3\text{O}_4$ -CMSC-5FU nanoparticles confirmed their ferromagnetic behavior. The saturation magnetization ( $M_s$ ) reduced from 53.45 emu/g for the  $\text{Fe}_3\text{O}_4$ - $\text{NH}_2$  nanoparticles to 42.32 emu/g for the 5-FU-conjugated  $\text{Fe}_3\text{O}_4$ - $\text{NH}_2$  nanoparticles. Increasing the concentration of CMSC reduced the magnetization from 26.35 to 5.89 emu/g. The  $r_1$  relaxation time and  $r_2$  relaxation time were 4.654 and 89.485  $\text{mM}^{-1}\text{s}^{-1}$ , respectively, which confirmed that the  $\text{Fe}_3\text{O}_4$ -CMSC-5FU nanoparticles could be used as a  $T_2$  contrasting agent for MRI imaging.

The drug release profile exhibited that at pH 5.4, 100% of 5-FU was released within 48 h, whereas and 0–20% of 5-FU was released at pH 7.2 in the same period. This pH-responsive release profile makes it more feasible for cancer treatment and achieving more target-specific therapy. The  $\text{Fe}_3\text{O}_4$ -CMSC-5FU was able to enter efficiently into the HeLa cells and HEK cells owing to its stability when compared with  $\text{Fe}_3\text{O}_4$ - $\text{NH}_2$ . After 12-h incubation, the cells containing  $\text{Fe}_3\text{O}_4$ -CMSC-5FU underwent cellular apoptosis, which prevented cell proliferation. However, the cells containing  $\text{Fe}_3\text{O}_4$ - $\text{NH}_2$  had no or minimal cell death when compared with the control.

The biodistribution of the ICG-labeled nanoparticles proved that magnetic targeting could be used to localize the nanoparticles in the tumor region. Thus, making it is evident that the  $\text{Fe}_3\text{O}_4$ -CMSC-5FU nanoparticles can be localized using the external magnetic field.

A remarkable increase in the temperature of the outside tissue from  $24^\circ\text{C}$  to  $92^\circ\text{C}$  was observed in the human cervical carcinoma cells loaded with  $\text{Fe}_3\text{O}_4$ -CMSC-5FU at a concentration of 300 mg/mL under irradiation for 975 s using 808 nm laser with a power density of  $600 \text{ mW}/\text{cm}^2$ . This proved that  $\text{Fe}_3\text{O}_4$  can absorb NIR light and transfer it to heat energy very efficiently. The in vivo studies revealed that the combination therapy involving  $\text{Fe}_3\text{O}_4$ -CMSC-5FU nanoparticles, along with NIR laser treatment, led to a notable increase in temperature within the cancer tissue site. The continuous growth of interest in nano drug delivery systems for cancer therapy and diagnosis underscores the potential of nanotechnology to revolutionize cancer treatment by offering more targeted, effective, and less toxic therapies. However, it is important to note that while significant progress has been made, challenges remain, particularly regarding clinical translation and scalability of these nano-based approaches. The  $\text{Fe}_3\text{O}_4$ -CMSC-5FU nanoparticles can be effectively exploited for oncological applications, with proven therapeutic, diagnostic and prognostic benefits.

### Supplementary Information

The online version contains supplementary material available at <https://doi.org/10.1186/s12645-024-00254-6>.

**Additional file 1: Figure S1.** X-ray diffraction pattern of  $\text{Fe}_3\text{O}_4$ - $\text{NH}_2$ ,  $\text{Fe}_3\text{O}_4$ -CMSC,  $\text{Fe}_3\text{O}_4$ -5FU,  $\text{Fe}_3\text{O}_4$ -CMSC-5FU ( $F^1$ ,  $F^3$ ) nanoparticles.

### Acknowledgements

The authors also would like to gratefully acknowledge the technical staffs of Malaysia Nuclear Agency for assistance for the animal study facilities.

### Author contributions

AKV: investigation, conceptualization, methodology, data curation, formal analysis writing original draft; TS: conceptualization, methodology; RP: writing—review and editing, data curation; SM: methodology, project administration, data curation, writing—review and editing; SBK: conceptualization, methodology; LYY: validation, visualization; PJ: supervision, project administration, validation, visualization, writing—review and editing, submission.

### Funding

E-Science Fund (06-02-10-SF0089) from the Malaysian Ministry of Science, Technology and Innovation. School of Science, Monash University Malaysia provided support for the research work through the Higher Degree Research (HDR) student fund.

### Availability of data and materials

The data will be available if needed.

### Declarations

#### Ethics approval consent to participate

Ethical clearance approved by Universiti Kebangsaan Malaysia (UKM) Laboratory Animal Center (MONASH/2016/PUSHPAMALAR/28-JAN./721-MARCH-2016-MAY-2016) and Monash University field work approval (MARF/2106/084/FW) by Monash Animal Ethics Committee.

#### Consent for publication

All authors mutually agreed with the publication of this manuscript in this journal.

#### Competing interests

The author declares no competing of interest.

Received: 30 October 2023 Accepted: 14 February 2024

Published online: 16 March 2024

### References

- Adam A, Mertz D (2023) Iron oxide@ mesoporous silica Core-Shell nanoparticles as multimodal platforms for magnetic resonance imaging, magnetic hyperthermia, near-infrared light Photothermia, and drug delivery. *Nanomaterials* 13(8):1342
- Agostinis P, Berg K, Cengel KA, Foster TH, Girotti AW, Gollnick SO, Hahn SM, Hamblin MR, Juzeniene A, Kessel D et al (2011) Photodynamic therapy of cancer: an update. *CA Cancer J Clin* 61(4):250–281
- Arsalani N, Fattahi H, Nazarpour M (2010) Synthesis and characterization of PVP-functionalized superparamagnetic Fe<sub>3</sub>O<sub>4</sub> nanoparticles as an MRI contrast agent. *Express Polym Lett* 4(6):329–338
- Artopoulos II, Chambers MS, Zinelis S, Eliades G (2016) Peel strength and interfacial characterization of maxillofacial silicone elastomers bonded to titanium. *Dent Mater* 32(7):e137–e147
- Bertrand J-C, Caumette P, Lebaron P, Matheron R, Normand P, Ngando TS (2015) *Environmental microbiology: fundamentals and applications*; Springer
- Chauhan P, Kushwaha P (2021) Applications of iron oxide nanoparticles in magnetic resonance imaging (MRI). *Nanosci Nanotechnol* 11(3):290–299
- Chen S, Li Y, Guo C, Wang J, Ma J, Liang X, Yang L-R, Liu H-Z (2007) Temperature-responsive magnetite/PEO–PPO–PEO block copolymer nanoparticles for controlled drug targeting delivery. *Langmuir* 23(25):12669–12676
- Chen L, Yu Q, Cheng K, Topham PD, Xu M, Sun X, Pan Y, Jia Y, Wang S, Wang L (2021) Can photothermal post-operative cancer treatment be induced by a thermal trigger? *ACS Appl Mater Interfaces* 13(51):60837–60851
- Choong N, Vokes E (2008) Expanding role of the medical oncologist in the management of head and neck cancer. *CA Cancer J Clin* 58(1):32–53
- Corot C, Robert P, Idée J-M, Port M (2006) Recent advances in iron oxide nanocrystal technology for medical imaging. *Adv Drug Deliv Rev* 58(14):1471–1504
- Danhier F, Danhier P, Schleich N, Po C, Laurent S, Sibret P, Jérôme C, Pouchelle V, Gallez B, Préat V (2018) Tumor targeting by RGD-grafted PLGA-based nanotheranostics loaded with Paclitaxel and superparamagnetic iron oxides. *Integrin Target Syst Tumor Diagn Ther.* 1–17.
- De Gramont A, Vignoud J, Tournigand C, Louvet C, Andre T, Varette C, Raymond E, Moreau S, Le Bail N, Krulik M (1997) Oxaliplatin with high-dose leucovorin and 5-fluorouracil 48-hour continuous infusion in pretreated metastatic colorectal cancer. *Eur J Cancer* 33(2):214–219
- Dominguez-Brauer C, Thu KL, Mason JM, Blaser H, Bray MR, Mak TW (2015) Targeting mitosis in cancer: emerging strategies. *Mol Cell* 60(4):524–536
- El-Damrawi G, Kamal H, Doweidar H, Dawood A (2016) Microstructure and in vitro bioactivity of metal substituted hydroxyapatite. *Br J Appl Sci Technol* 15(2):1
- El-Sherbiny IM, El-Sayed M, Reda A (2020) Superparamagnetic iron oxide nanoparticles (SPIONs) as multifunctional cancer theranostics. *Magnetic nanoheterostructures: diagnostic, imaging and treatment.* 223–241
- Espinosa A, Di Corato R, Kolosnjaj-Tabi J, Flaud P, Pellegrino T, Wilhelm C (2016) Duality of iron oxide nanoparticles in cancer therapy: amplification of heating efficiency by magnetic hyperthermia and photothermal bimodal treatment. *ACS Nano* 10(2):2436–2446
- Fernandes DA, Appak-Baskoy S, Berndt E, Kolios MC (2021a) Laser activatable perfluorocarbon bubbles for imaging and therapy through enhanced absorption from coupled silica coated gold nanoparticles. *RSC Adv* 11(9):4906–4920
- Fernandes DA, Fernandes DD, Malik A, Gomes GNW, Appak-Baskoy S, Berndt E, Gradinaru CC, Kolios MC (2021b) Multifunctional nanoparticles as theranostic agents for therapy and imaging of breast cancer. *J Photochem Photobiol B Biol* 218:112110
- Freedman D (1990) *Statistics Department University of California.*
- Garnacho C (2016) Intracellular drug delivery: mechanisms for cell entry. *Curr Pharm Des* 22(9):1210–1226

- Gautam V, Srivastava A, Singh KP, Yadav VL (2016) Vibrational and gravimetric analysis of polyaniline/polysaccharide composite materials. *Polym Sci, Ser A* 58:206–219
- Gupta AK, Gupta M (2005) Synthesis and surface engineering of iron oxide nanoparticles for biomedical applications. *Biomaterials* 26(18):3995–4021
- Hamidi M, Azadi A, Rafiei P, Ashrafi H (2013) A pharmacokinetic overview of nanotechnology-based drug delivery systems: an ADME-oriented approach. *Crit Rev Ther Drug Carrier Syst* 30(5):435
- Hola K, Markova Z, Zoppellaro G, Tucek J, Zboril R (2015) Tailored functionalization of iron oxide nanoparticles for MRI, drug delivery, magnetic separation and immobilization of biosubstances. *Biotechnol Adv* 33(6):1162–1176
- Hooshmand S, Hayat SM, Ghorbani A, Khatami M, Pakravanan K, Darroudi M (2021) Preparation and applications of superparamagnetic iron oxide nanoparticles in novel drug delivery systems: an overview. *Curr Med Chem* 28(4):777–799
- Kango S, Kalia S, Celli A, Njuguna J, Habibi Y, Kumar R (2013) Surface modification of inorganic nanoparticles for development of organic–inorganic nanocomposites—a review. *Prog Polym Sci* 38(8):1232–1261
- Kato Y, Zhu W, Backer MV, Neoh CC, Hapuarachchige S, Sarkar SK, Backer JM, Artemov D (2015) Noninvasive imaging of liposomal delivery of superparamagnetic iron oxide nanoparticles to orthotopic human breast tumor in mice. *Pharm Res* 32:3746–3755
- Lu X, Zhou H, Liang Z, Feng J, Lu Y, Huang L, Qiu X, Xu Y, Shen Z (2022) Biodegradable and biocompatible exceedingly small magnetic iron oxide nanoparticles for T1-weighted magnetic resonance imaging of tumors. *J Nanobiotechnol* 20(1):1–11
- Madamsetty VS, Mukherjee A, Mukherjee S (2019) Recent trends of the bio-inspired nanoparticles in cancer theranostics. *Front Pharmacol* 10:1264
- Mahmoudi M, Sant S, Wang B, Laurent S, Sen T (2011) Superparamagnetic iron oxide nanoparticles (SPIONs): development, surface modification and applications in chemotherapy. *Adv Drug Deliv Rev* 63(1):24–46
- Monopoli MP, Aberg C, Salvati A, Dawson KA (2020) Biomolecular coronas provide the biological identity of nanosized materials. *Nano Enabled Med Appl*. 205–229
- Motofei IG (2023) Biology of cancer; understanding the supracellular control of mitosis in physiological processes and malignancy. *Semin Cancer Biol* 92:42
- Murgja S, Falchi AM, Mano M, Lampis S, Angius R, Carnerup AM, Schmidt J, Diaz G, Giacca M, Talmon Y (2010) Nanoparticles from lipid-based liquid crystals: emulsifier influence on morphology and cytotoxicity. *J Phys Chem B* 114(10):3518–3525
- Nemec S, Kralj S, Wilhelm C, Abou-Hassan A, Rols M-P, Kolosnjaj-Tabi J (2020) Comparison of iron oxide nanoparticles in photothermia and magnetic hyperthermia: effects of clustering and silica encapsulation on nanoparticles' heating yield. *Appl Sci* 10(20):7322
- Stanicki D, Vangijzegem T, Ternad I, Laurent S (2022) An update on the applications and characteristics of magnetic iron oxide nanoparticles for drug delivery. *Expert Opin Drug Deliv* 19(3):321–335
- Stark WJ, Stoessel PR, Wohlleben W, Hafner A (2015) Industrial applications of nanoparticles. *Chem Soc Rev* 44(16):5793–5805
- Sun L, Joh DY, Al-Zaki A, Stangl M, Murty S, Davis JJ, Baumann BC, Alonso-Basanta M, Kao GD, Tsurkas A (2016) Theranostic application of mixed gold and superparamagnetic iron oxide nanoparticle micelles in glioblastoma multiforme. *J Biomed Nanotechnol* 12(2):347–356
- Ulaganathan V, Retzlaff I, Won J, Gochev G, Gehin-Delval C, Leser M, Noskov B, Miller R (2017)  $\beta$ -Lactoglobulin adsorption layers at the water/air surface: 1. Adsorption kinetics and surface pressure isotherm: effect of pH and ionic strength. *Colloids Surf A Physicochem Eng Aspects* 519:153–160
- Verma A, Stellacci F (2010) Effect of surface properties on nanoparticle–cell interactions. *Small* 6(1):12–21
- Wei Y, Liao R, Liu H, Li H, Xu H, Zhou Q (2015) Biocompatible low-retention superparamagnetic iron oxide nanoclusters as contrast agents for magnetic resonance imaging of liver tumor. *J Biomed Nanotechnol* 11(5):854–864
- Xu Z, Hou Y, Sun S (2007) Magnetic core/shell Fe<sub>3</sub>O<sub>4</sub>/Au and Fe<sub>3</sub>O<sub>4</sub>/Au/Ag nanoparticles with tunable plasmonic properties. *J Am Chem Soc* 129(28):8698–8699
- Xu X, Ho W, Zhang X, Bertrand N, Farokhzad O (2015) Cancer nanomedicine: from targeted delivery to combination therapy. *Trends Mol Med* 21(4):223–232
- Yang Y, Liu J, Liang C, Feng L, Fu T, Dong Z, Chao Y, Li Y, Lu G, Chen M (2016) Nanoscale metal–organic particles with rapid clearance for magnetic resonance imaging-guided photothermal therapy. *ACS Nano* 10(2):2774–2781
- Yang J, Feng J, Yang S, Xu Y, Shen Z (2023) Exceedingly small magnetic iron oxide nanoparticles for T1-weighted magnetic resonance imaging and imaging-guided therapy of tumors. *Small* 19(49):2302856
- Yu J, Yin W, Zheng X, Tian G, Zhang X, Bao T, Dong X, Wang Z, Gu Z, Ma X (2015) Smart MoS<sub>2</sub>/Fe<sub>3</sub>O<sub>4</sub> nanotheranostic for magnetically targeted photothermal therapy guided by magnetic resonance/photoacoustic imaging. *Theranostics* 5(9):931

## Publisher's Note

Springer Nature remains neutral with regard to jurisdictional claims in published maps and institutional affiliations.